

Valence-band mixing in first-principles envelope-function theory

Bradley A. Foreman

Department of Physics, Hong Kong University of Science and Technology, Clear Water Bay, Kowloon, Hong Kong, China

This paper presents a numerical implementation of a first-principles envelope-function theory derived recently by the author [B.A. Foreman, *Phys. Rev. B* 72, 165345 (2005)]. The examples studied deal with the valence subband structure of $\text{GaAs/Al}_0.2\text{Ga}_{0.8}\text{As}$ and $\text{In}_{0.53}\text{Ga}_{0.47}\text{As/InP}$ (001) superlattices calculated using the local density approximation to density-functional theory and norm-conserving pseudopotentials without spin-orbit coupling. The heterostructure Hamiltonian is approximated using quadratic response theory, with the heterostructure treated as a perturbation of a bulk reference crystal. The valence subband structure is reproduced accurately over a wide energy range by a multiband envelope-function Hamiltonian with linear renormalization of the momentum and mass parameters. Good results are also obtained over a more limited energy range from a single-band model with quadratic renormalization. The effective kinetic-energy operator ordering derived here is more complicated than in many previous studies, consisting in general of a linear combination of all possible operator orderings. In some cases the valence-band Rashba coupling differs significantly from the bulk magnetic Luttinger parameter. The splitting of the quasidegenerate ground state of non-coupled atom superlattices has non-negligible contributions from both short-range interface mixing and long-range dipole terms in the quadratic density response.

PACS numbers: 73.21.b, 73.61.Ey, 71.15.Ap

I. INTRODUCTION

In a recent paper, the author has developed a first-principles multiband envelope-function theory for semiconductor heterostructures.¹ This theory can in principle provide accurate numerical predictions of envelope-function Hamiltonian parameters, but only if a reliable quasiparticle self-energy is used as input. On the other hand, if the input potential is taken from a simple density-functional calculation, the numerical values are less accurate, but the theory can still provide deep insight into the basic physics of the interface and clarify various limitations of commonly used envelope-function models. The purpose of the present article is to explore these topics using numerical examples taken from density-functional calculations of the valence subband structure in semiconductor superlattices.

In order to obtain the most direct comparison with envelope-function theory as it is commonly used, the Hamiltonian was derived in Ref. 1 in the form of a matrix containing differential operators and energy-independent functions of position. Using a differential equation of low order to describe an abrupt heterojunction might seem at first glance to be a gross theoretical blunder, since it is well known that bulk effective-mass theory² is valid only for slowly varying perturbing potentials. Yet effective-mass theory is widely accepted as a valid lowest-order approximation for the shallow impurity problem,³ even though the atomic impurity potential is not slowly varying. Its validity in this context is established by the existence of rigorous methods for extending effective-mass theory to include higher-order perturbations,⁴ including the rapidly varying part of the impurity potential.⁵ These produce short-range and long-range corrections to the effective Hamiltonian (each with its own independent parameters), which lead to the well-known chem-

ical shift and splitting of effective-mass degeneracies,⁵ thereby bringing the rough estimates of effective-mass theory into much closer agreement with experiment.

A heterostructure is nothing but an assembly of atoms. It is therefore difficult to imagine a valid argument for accepting the use of generalized effective-mass differential equations in the shallow impurity problem, yet categorically rejecting them for small atomic perturbations in heterostructures. According to linear response theory, the perturbation generated by a collection of small atomic perturbations is to leading order just the superposition of the individual perturbations. The rapidly varying part of the heterostructure potential^{6,7} can thus be handled by the same techniques used in the impurity problem.⁵ The validity of low-order differential equations for shallow heterostructures, as for shallow impurities, consequently rests on two fundamental assumptions:^{2,5} that the envelope functions satisfying these equations are slowly varying⁶ (i.e., have a Fourier transform limited to small wave vectors) within the energy range of experimental interest, and that the atomic perturbations are truly "shallow" in real heterostructures.

The first assumption is confirmed by numerical examples in later sections of this paper, in agreement with empirical pseudopotential studies.^{8,9,10,11} For the second assumption, the definition of "shallow" is a relative one that depends on the energy separation between the states included explicitly in the envelope-function model and the remote states treated as perturbations [see, e.g., Eq. (II.33) of Ref. 2]. Consider the case of a $\text{GaAs/Al}_0.5\text{Ga}_{0.5}\text{As}$ heterostructure, where the valence-band offset is about 0.5 eV and the energy gap is about 1.5 eV. Treating $\text{GaAs/Al}_0.5\text{Ga}_{0.5}\text{As}$ as a shallow perturbation of the virtual crystal $\text{Al}_0.5\text{Ga}_{0.5}\text{As}$ would be expected to yield marginal results (at best) in a single-band effective-mass model for the degenerate valence states. Such a model would

be expected to give good results only for weaker perturbations, such as those in a GaAs/Al_{0.2}Ga_{0.8}As heterostructure (within the virtual-crystal approximation). On the other hand, treating GaAs/AlAs as a shallow perturbation would be expected to produce good results in a multiband envelope-function model that includes a few of the nearest conduction-band states explicitly, since the remote bands are then more than 5 eV away from the valence-band maximum. (This method of making "deep" perturbations "shallow" by including more bands in the Hamiltonian was proposed by Keldysh for the deep impurity problem in bulk semiconductors.¹²) All of the above expectations are confirmed below by numerical examples for GaAs/Al_{0.2}Ga_{0.8}As, GaAs/AlAs, and In_{0.53}Ga_{0.47}As/InP.

To be more specific, the multiband envelope-function Hamiltonian of Ref. 1 was derived by treating the heterostructure as a perturbation (within the pseudopotential approximation) of a virtual bulk reference crystal. The self-consistent potential energy of the heterostructure was approximated using the linear and quadratic terms of nonlinear response theory. A finite-order envelope-function Hamiltonian was constructed by using Luttinger-Kohn perturbation theory^{2,5,13,14} to eliminate the $k \cdot p$ and potential-energy coupling to remote bands, working to order k^4 in the bulk reference Hamiltonian,⁷ to order k^2 in the linear response terms,^{13,14} and to order k^0 in the quadratic response.⁷ This theory is shown here to work well in a 3-state model for the ^{15}V valence states (i.e., neglecting spin-orbit coupling) of a GaAs/Al_{0.2}Ga_{0.8}As superlattice and in a 7-state $f_{15c},_{1c},_{15Vg}$ model for GaAs/AlAs and In_{0.53}Ga_{0.47}As/InP superlattices. Examples illustrating the success of a 4-state $f_{1c},_{15Vg}$ model for In_{0.53}Ga_{0.47}As/InP superlattices have been given elsewhere.¹⁵

To test the limits of the single-band (^{15}V) model, this paper also extends the theory of Ref. 1 to include terms of order 2k and $^2k^2$, where denotes the heterostructure perturbation. This is shown to yield much better predictions of the position-dependent effective masses of both GaAs/AlAs and In_{0.53}Ga_{0.47}As/InP than the $O(^1k^2)$ theory of Ref. 1. The resulting superlattice band structures are also of reasonably good accuracy, but over a more limited energy range than the multiband models. The principal limitation of the single-band theory seems to be the presence of spurious solutions generated by $O(^0k^4)$ terms in the bulk reference Hamiltonian.

The extended $O(^2k^2)$ theory also yields some interesting conclusions regarding operator ordering in the effective kinetic-energy operator T in effective-mass theory. Much previous work has examined various possible ways of choosing the exponents α, β , and γ in the von Roos parameterization¹⁶

$$T_{VR} = \frac{1}{4} (m_{\perp} p_{\perp}^2 + m_{\parallel} p_{\parallel}^2); \quad (1)$$

where p is the momentum operator (in one dimension), m is the effective mass, and $\alpha + \beta + \gamma = 1$. Morow and

Brownstein^{17,18} have argued that only exponents satisfying $\alpha = \beta = \gamma$ are physically permissible in abrupt heterostructures, which would rule out seemingly reasonable possibilities such as¹⁹ $T = \frac{1}{4} (m_{\perp}^{-1} p_{\perp}^2 + m_{\parallel}^{-1} p_{\parallel}^2)$.

The present theory is not consistent with any single operator ordering of this type. Instead, the terms of order p^2 derived here take the form of a linear combination of terms containing position-dependent functions having all possible operator orderings with respect to p . The apparent conflict between this result and the theory of Morow and Brownstein^{17,18} is resolved by the fact that these are smooth functions of position with no discontinuity even at an abrupt junction.

The structure of the paper is as follows. The choices made in defining the model system used for numerical calculations are described in Sec. II. Section III outlines the methods used to calculate the linear and quadratic response to the heterostructure perturbation and discusses the physical significance of the results. Section IV describes the construction of the envelope-function Hamiltonian, which is also studied from the perspective of the theory of invariants. In Sec. V, the parameters of the Hamiltonian are calculated and discussed for the material systems GaAs/AlAs, GaAs/Al_{0.2}Ga_{0.8}As, and In_{0.53}Ga_{0.47}As/InP. The valence subband structures for (001) superlattices of these materials are calculated in Sec. VI, which compares the predictions of various approximate envelope-function models with "exact" numerical calculations. Finally, the results of the paper are discussed and summarized in Sec. VII.

II. CHOICE OF MODEL

All of the numerical results in this paper are derived from plane-wave pseudopotential total-energy calculations^{20,21} performed using the ab initio software.^{22,23,24} This package provides a variety of options, but the particular calculations reported here used the nonlocal norm-conserving pseudopotentials of Hartwigsen, Goedecker, and Hutter²⁵ and Teter's Padé interpolation of Ceperley-Alder exchange-correlation data²⁶ within the local density approximation (LDA) to density-functional theory.

Choosing a particular physical structure and a particular set of technical ingredients (such as plane-wave kinetic-energy cuts and k -point sampling) defines a model system whose properties can be calculated self-consistently to an accuracy approaching that of machine precision. These "exact" model calculations are used here as a benchmark for comparison with various approximations used in the construction of the envelope-function theory of Ref. 1. The main objective of this paper is to pin down as closely as possible how much error arises from these approximations. With this goal in mind, several compromises have been made in the definition of the model system that are not ideal if one wishes to achieve the closest approximation to physical reality.

First, *ab initio* calculations of the quasiparticle self-energy in the GW approximation.^{27,28} This would provide more accurate conduction bands than LDA calculations, but the computational cost is prohibitive for the relatively large superlattices in which envelope-function theory is valid. Therefore, only the valence bands are examined in detail in this paper.

Second, although spin-orbit coupling can be included in *ab initio*, in the existing implementation it cannot yet be used together with the virtual-crystal pseudopotentials needed to apply the nonlinear response theory of Ref. 1. Therefore, to avoid a complete restructuring of the basic code, spin-orbit coupling was omitted. This means that "spintronic" features cannot be studied directly; however, closely related "orbitronics" effects²⁹ arising from the orbital angular momentum of the valence states can be studied within the context of the valence-band Rashba Hamiltonian (see Sec. IV).

Third, since large supercells are used, relatively low kinetic-energy cutoffs (see below) and numbers of special k points were chosen. In particular, two independent k points were used for GaAs/AlAs superlattices with D_{2d} symmetry, while four points were used for $In_{0.53}Ga_{0.47}As/InP$ superlattices with C_{2v} symmetry. The total energy is not completely converged at these values, but the valence-band offsets calculated here are nevertheless in good agreement with previous first-principles calculations reported in the literature.

Fourth, in order to calculate multipole moments of the linear and quadratic response, it is necessary that the electron density and short-range potential response be well localized within the given large supercells. However, sharp cutoffs in the plane-wave basis produce spurious long-range Gibbs oscillations that are very small but nonetheless large enough to completely swamp the physical multipole values. To suppress these oscillations, the smoothening functions shown in Fig. 1 were applied to the kinetic and potential energy. The kinetic energy divisor shown is already included in the *ab initio* package, while a similar smoothening function of higher order was used for the local and nonlocal potential energy. (One could avoid the need for pseudopotential smoothening by using hard-coded analytical derivatives of the pseudopotentials in k space rather than numerically evaluated multipole moments, but this was not done here as it would require separate coding for each pseudopotential parameterization.) The chosen kinetic-energy cutoff (i.e., the value at which the divisor in Fig. 1 goes to zero) includes 283 plane waves at the point in bulk material (113 of which are not altered by smoothening) and more than 14000 plane waves in a 96-atom superlattice.

In principle, one could calculate the linear and quadratic response much more efficiently than the direct supercell method adopted here³⁰ by using the techniques of density-functional perturbation theory.³¹ However, this is not yet encoded in *ab initio* for the "virtual alchemy" perturbations needed here.²² This would certainly be the method of choice for realistic predictions

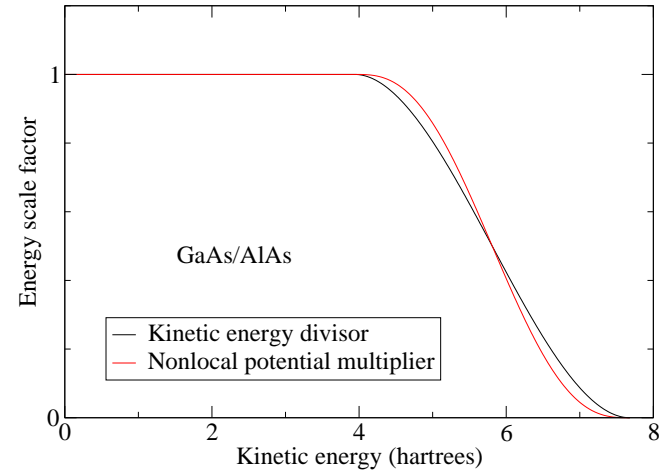


FIG. 1: (Color online) Kinetic energy divisor (with continuous slope) and nonlocal potential energy multiplier (with continuous curvature) used to smooth out discontinuities in the momentum-space electron density and pseudopotential. The multiplier used for the local pseudopotential has the same shape, but the energy scale is four times that shown.

of envelope-function Hamiltonian parameters, since it avoids the need for supercell calculations, thereby permitting larger plane-wave cutoffs (with no smoothening necessary) and numbers of special k points, and possibly even GW self-energies. However, this would also introduce some uncertainty into comparisons of envelope-function predictions with "exact" model calculations on superlattices, since the technical ingredients used to calculate the parameters would not be feasible for use in the exact calculation.

III. CALCULATION OF THE LINEAR AND QUADRATIC RESPONSE

A. Conventions defining the absolute energy

There are two conventions in *ab initio* that determine the absolute value of the local potential. First, the mean value of the Hartree potential is set to zero by definition.^{32,33,34}

$$V_{H\text{ar}}(q) = (1 - \frac{q}{q_0}) \frac{4}{q^2} n(q) \quad (2)$$

(where n is the valence electron density), because in a neutral system the net contribution to the total energy from the Coulomb interaction terms (for the electron-ion system) at wave vector $q = 0$ is identically zero.

A similar convention³² is used for the mean value of the short-range part of the local pseudopotential. This is given by $V_{PSP} = \frac{1}{Z} \sum_j V_j$, where^{20,21,32,33,35}

$$V_j = \frac{1}{Z} \sum_{i=1}^Z V_j(r_i) + \frac{Z_j}{r} \int d^3r; \quad (3)$$

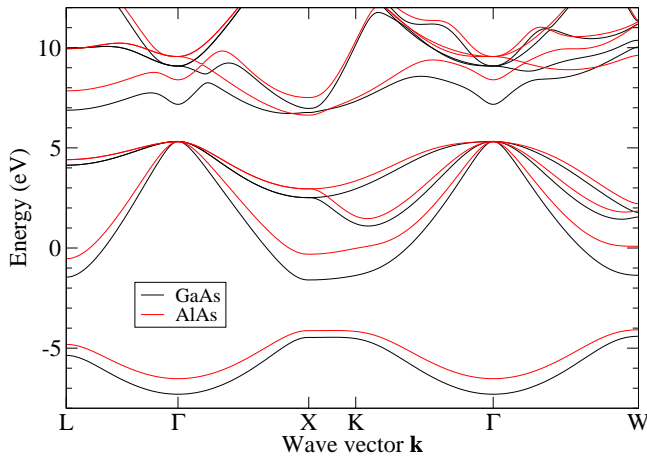


FIG. 2: (Color online) Energy band structure of bulk GaAs and AlAs.

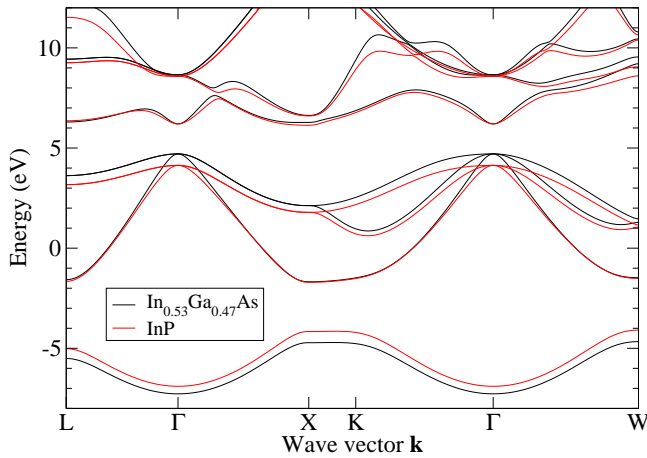


FIG. 3: (Color online) Energy band structure of bulk $\text{In}_{0.53}\text{Ga}_{0.47}\text{As}$ and InP.

in which v is the unit cell volume and V_j and Z_j are the local pseudopotential and valence charge of ion j . The contribution from V_{psp} to the total energy is just the constant $E_{\text{core}} = Z \cdot V_{\text{psp}}$, where $Z = \sum_j Z_j$. Hence, V_{psp} can be set to zero in the Kohn-Sham equations.³²

In order to calculate the nonlinear response correctly, V_{psp} must be included in the local pseudopotential. In the present work, this value was obtained from the internal ab initio variable core and added to both the local pseudopotential and all energy band structures calculated by ab initio. Therefore, the absolute energy scale for all figures in this paper is defined solely by the convention of setting the mean Hartree potential to zero.

Energy band structures for the model system described in Sec. II are presented in Figs. 2 and 3 for the bulk materials GaAs, AlAs, $\text{In}_{0.53}\text{Ga}_{0.47}\text{As}$, and InP. The conduction bands in these figures are clearly not realistic, as the minimum at L lies slightly below the minimum in GaAs, and is only slightly above it in $\text{In}_{0.53}\text{Ga}_{0.47}\text{As}$ and InP. The calculated $E_{\text{1c}} - E_{\text{1v}}$ energy gaps are 1.850

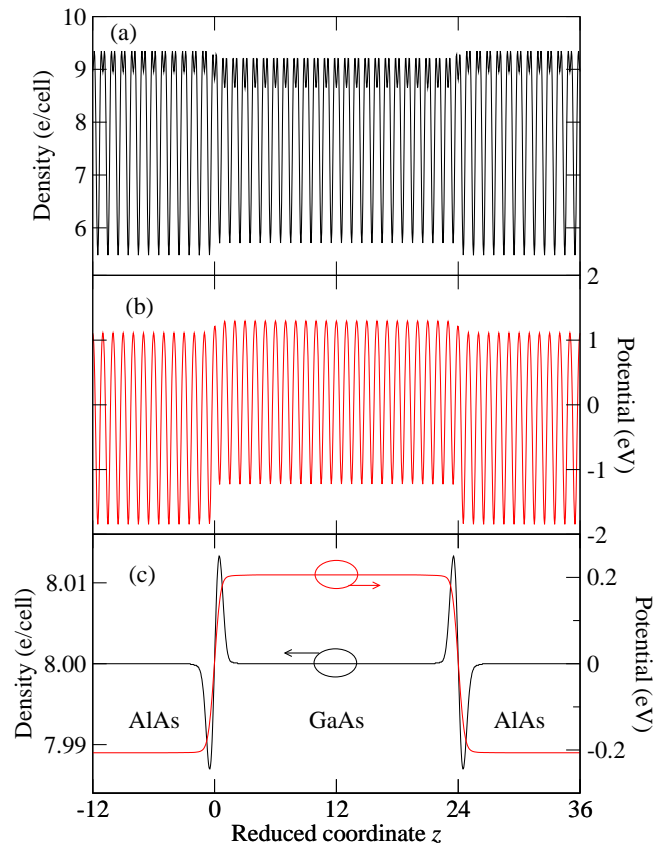


FIG. 4: (Color online) Density and potential of a (001) $(\text{GaAs})_{24}/\text{AlAs}_{24}$ superlattice: (a) Planar average of electron density. (b) Planar average of Hartree potential. (c) Macroscopic average of density and potential.

eV for GaAs and 1.492 eV for $\text{In}_{0.53}\text{Ga}_{0.47}\text{As}$, which are 13% and 61% larger than the experimental values³⁶ (with spin-orbit splitting removed) of 1.633 eV and 0.925 eV. Nevertheless, the model does capture many of the gross qualitative trends in experimentally determined band structures,³⁷ such as the predominance of the X valley in AlAs relative to GaAs.

It is important to note that the difference between the valence-band maxima in Figs. 2 and 3 is not equal to the valence-band offset.³⁸ To obtain the valence-band offset, one must add to this difference the shift in the macroscopic Hartree potential of the two materials as given by a supercell calculation.³⁸ The latter shift is shown in Figs. 4 and 5 for a GaAs/AlAs superlattice and in Figs. 6 and 7 for an $\text{In}_{0.53}\text{Ga}_{0.47}\text{As}/\text{InP}$ superlattice. These figures show planar averages and macroscopic averages^{39,40,41,42} of the electron density and Hartree potential. The macroscopic density for GaAs/AlAs in Fig. 4(c) has the familiar interface dipole shape,^{38,39} leading to a step-like shift in the Hartree potential of 0.412 eV. The shift predicted by linear response theory is very close to this value, at 0.416 eV (see below for a more detailed study of the error in this approximation). These results agree well with the shift of 0.41 eV calculated in Ref. 38. Since the difference

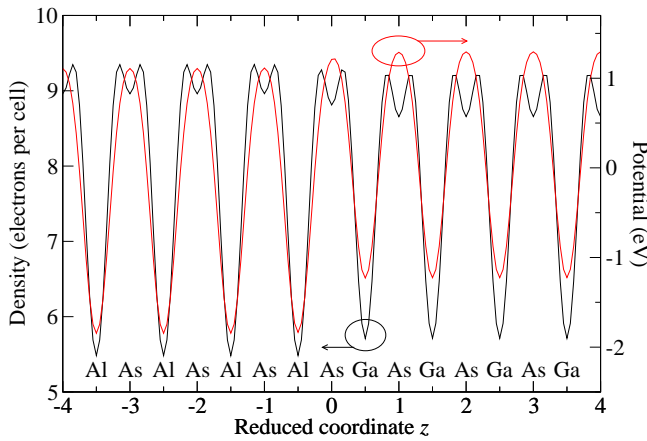


FIG. 5: (Color online) Expanded view of the planar average density and potential from Fig. 4.

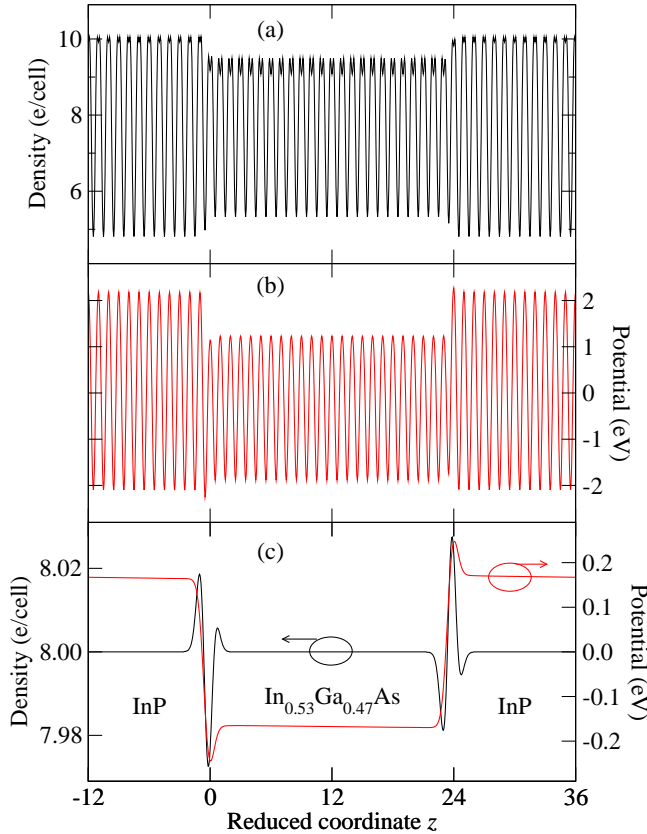


FIG. 6: (Color online) Density and potential of a (001) $(In_{0.53}Ga_{0.47}As)_{24}(InP)_{24}$ superlattice: (a) Planar average of electron density. (b) Planar average of Hartree potential. (c) Macroscopic average of density and potential.

between the valence-band maxima in Fig. 2 is 18 m eV, the valence-band offset for a (001) GaAs/AlAs heterojunction is 0.430 eV for the model system, as compared to the value of 0.45 eV reported in Ref. 38. If this figure is corrected for spin-orbit coupling and quasiparticle effects using the values in Ref. 38, the net offset is roughly 0.56

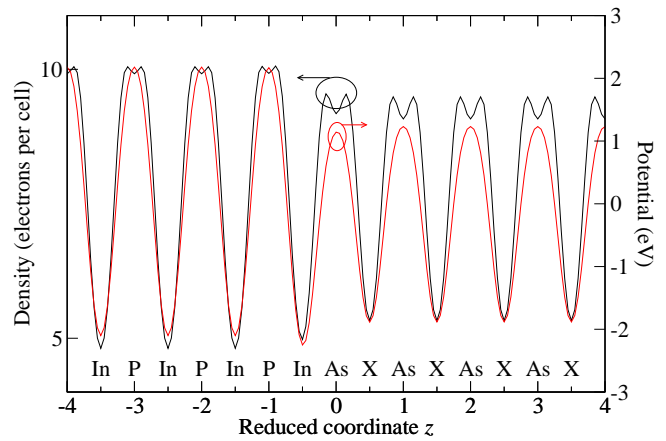


FIG. 7: (Color online) Expanded view of the planar average density and potential from Fig. 6. Here X represents the virtual atom $In_{0.53}Ga_{0.47}As$.

eV, in good agreement with the experimental value³⁶ of 0.53 eV.

The macroscopic density of the no-common-atom $In_{0.53}Ga_{0.47}As/InP$ superlattice in Fig. 6(c) does not have a simple dipole shape because (to leading order) it is a superposition of two offset dipoles, one for the cation and one for the anion.^{38,43} As discussed below, there is also a slight asymmetry of the two interfaces, leading to a macroscopic electric field that is barely visible in Fig. 6(c). The linear Hartree shifts [from Eq. (14) with $l=0$] for cations and anions are +0.366 eV and 0.697 eV, as compared to the values of +0.34 eV and 0.58 eV reported in Refs. 38 and 43. The net linear Hartree shift of 0.331 eV agrees well with the mean shift of 0.334 eV in Fig. 6(c). Combining this with the 0.574 eV difference in the valence-band maxima of Fig. 3, the net valence-band offset for the model $In_{0.53}Ga_{0.47}As/InP$ system is 0.240 eV. After adjusting for experimental spin-orbit splitting,³⁶ the calculated offset of 0.313 eV is close to the experimental value³⁶ of 0.345 eV.

B. Linear and quadratic response

The envelope-function Hamiltonian of Ref. 1 is not calculated directly from the superlattice density and potential (since that would require a separate first-principles calculation for each new structure), but is instead obtained from the linear and quadratic response to virtual-crystal perturbations of a bulk reference crystal. The reference crystal is defined as the virtual-crystal average of the bulk constituents (e.g., $Al_{0.5}Ga_{0.5}As$ for GaAs/AlAs and $In_{0.765}Ga_{0.235}As_{0.5}P_{0.5}$ for $In_{0.53}Ga_{0.47}As/InP$), which is easily implemented in ab initio. The lattice constant for all calculations was fixed at the value obtained by minimizing the total energy of the reference crystal (i.e., $a = 10.5$ bohr for $Al_{0.5}Ga_{0.5}As$ and $a = 10.9$ bohr for $In_{0.765}Ga_{0.235}As_{0.5}P_{0.5}$).

The perturbation of the heterostructure relative to the reference crystal is defined by the change in pseudopotential

$$V_{\text{psp}}(x) = \sum_{R} \frac{x - R}{R} v_{\text{ion}}(x - R); \quad (4)$$

which is written as a local potential for simplicity (see Ref. 1 for the nonlocal case). Here $v_{\text{ion}}(x)$ is the ionic pseudopotential of atom R , R is the position of atom in unit cell R , and $\frac{x - R}{R}$ is the change in fractional weight of atom R in cell R of the heterostructure relative to the reference crystal. Since the total change in fractional weight at each site must add to zero, this can be rewritten as¹

$$V_{\text{psp}}(x) = \sum_{R} \frac{x - R}{R} v_{\text{ion}}(x - R); \quad (5)$$

where the sum covers only independent values of R (e.g., either Ga or Al but not both in GaAs/AlAs), and v_{ion} is the change in v_{ion} relative to the reference crystal.

If $n(x)$ is the exact density of the heterostructure, the linear and quadratic response to virtual perturbations R are defined as the derivatives

$$n_R(x) = \frac{\partial n(x)}{\partial R}; \quad (6a)$$

$$n_{RR^0}(x) = \frac{1}{2} \frac{\partial^2 n(x)}{\partial R \partial R^0}; \quad (6b)$$

The total density may then be reconstructed from the power series

$$n(x) = n^{(0)}(x) + n^{(1)}(x) + n^{(2)}(x) + \dots \quad (7a)$$

$$n^{(1)}(x) = \sum_{R} n_R(x); \quad (7b)$$

$$n^{(2)}(x) = \sum_{R} \frac{x - R}{R} n_{RR^0}(x); \quad (7c)$$

where $n^{(0)}(x)$ is the density of the reference crystal.

In the present calculations, this power series was truncated at the second order. If we consider for simplicity a function of only two variables, the density and potential are therefore written as quadratic functions

$$f(1; 2) = c + c_1 1 + c_2 2 + c_{11} 1^2 + c_{22} 2^2 + 2c_{12} 1 2; \quad (8)$$

Here the coefficients c , c_i , and c_{ij} were calculated by the direct supercell method.³⁰ First, the self-consistent density and potential were found for a supercell consisting of the reference crystal with a monatomic perturbation

$i = i$ (e.g., in $\text{Al}_{0.5}\text{Ga}_{0.5}\text{As}$, one $\text{Al}_{0.5}\text{Ga}_{0.5}$ atom was replaced by either $\text{Al}_{0.55}\text{Ga}_{0.45}$ or $\text{Al}_{0.45}\text{Ga}_{0.55}$). This provides the values of the coefficients

$$c = f_{00}; \quad (9a)$$

$$c_1 = \frac{f_{10} - f_{00}}{2 - 1}; \quad (9b)$$

$$c_{11} = \frac{f_{10} + f_{00} - 2f_{00}}{2 - 1^2}; \quad (9c)$$

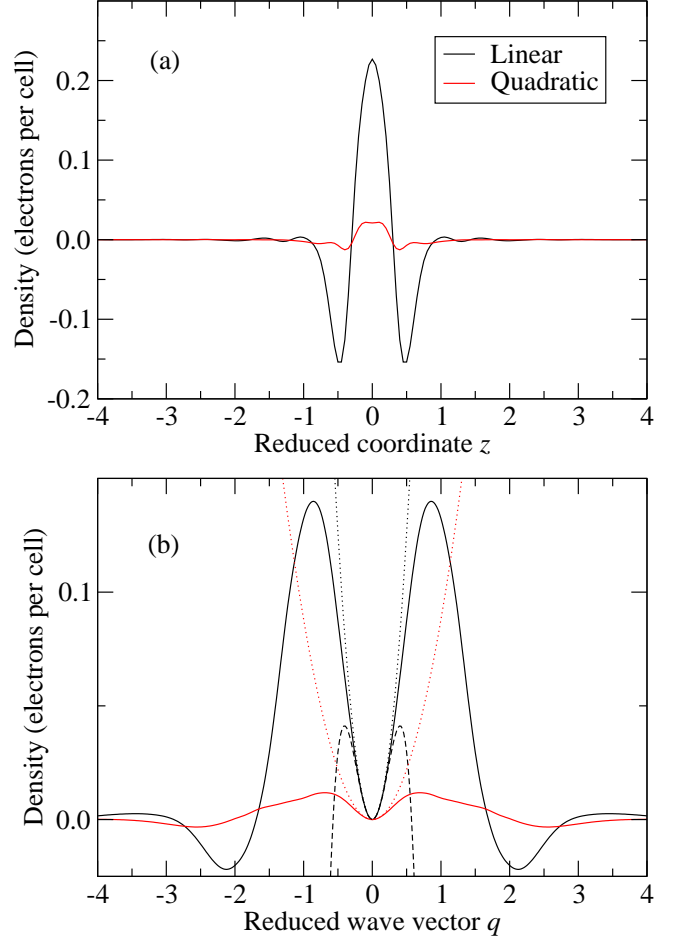


FIG. 8: (Color online) Linear and quadratic density response to a monatomic perturbation of $\text{Al}_{0.5}\text{Ga}_{0.5}\text{As}$: (a) coordinate space; (b) momentum space. In (b), the dotted and dashed lines are quadratic and quartic polynomials defined by the quadrupole and hexadecapole moments.

where $f_{10} = f(1; 0)$, etc. Next, diatomic perturbations were used to find the value of c_{12} . Two possible formulas were considered:

$$c_{12} = \frac{f_{11} - f_{10} - f_{01} + f_{00}}{8 - 1 - 2}; \quad (10a)$$

$$c_{12} = \frac{f_{11} - f_{10} - f_{01} + f_{00}}{2 - 1 - 2}; \quad (10b)$$

The symmetric formula (10a) is presumably more accurate, but very little difference was found in comparison to the asymmetric formula (10b). Since the latter requires only one-fourth the computation time and storage of the former, Eq. (10b) was used for all calculations reported here.

The linear and quadratic density response to a monatomic perturbation in $\text{Al}_{0.5}\text{Ga}_{0.5}\text{As}$ are shown in Fig. 8. The functions plotted in part (a) are planar averages of $n_R(x)$ and $n_{RR}(x)$ for the case $i = \text{Ga}$. Since the supercell used here is the same as that of the (001) superlattice in Figs. 4 and 5, the perturbation actually

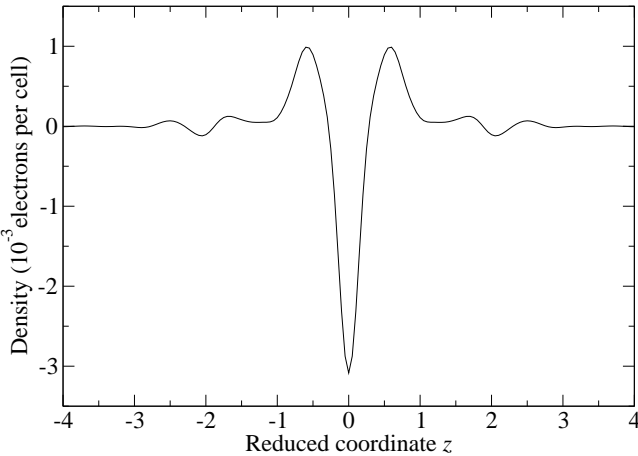


FIG. 9: Quadratic density response to a diatom ionic perturbation of $\text{Al}_{0.5}\text{Ga}_{0.5}\text{As}$. The perturbations are applied at $z = -0.5$ and $z = +0.5$.

consists of a plane of Ga atoms (or rather an in nitesimal perturbation toward Ga). This perturbation has D_{2d} symmetry, so the planar average shown in Fig. 8(a) is symmetric. Note that the quadratic response is about an order of magnitude smaller than the linear response.

The quadratic response to a diatom ionic perturbation in $\text{Al}_{0.5}\text{Ga}_{0.5}\text{As}$ is shown in Fig. 9. This perturbation also has D_{2d} symmetry, so its qualitative features are similar to those of the monatomic ionic response. The perturbation planes in Fig. 9 are separated by one monolayer (i.e., $\frac{1}{2}$ a). The calculations performed in this paper include diatom ionic perturbations out to a separation of four monolayers.

Qualitatively different results are obtained for the perturbation of two different atoms of the $\text{In}_{0.765}\text{Ga}_{0.235}\text{As}_{0.5}\text{P}_{0.5}$ reference crystal in Fig. 10. This diatom ionic perturbation has symmetry C_{2v} , so its planar average is not symmetric. It therefore has a nonvanishing dipole moment, which is readily apparent from the figure. The dipole generates a rapid change in the Hartree potential, as shown in Fig. 10(b). In order to satisfy the periodic boundary conditions, this steplike change in potential must be accompanied by a macroscopic electric field extending over the entire supercell. This field polarizes the reference crystal, producing small oscillations in the density and potential⁴⁴ that are visible away from $z = 0$. Figure 10 shows calculations performed on two supercells, one with 48 monolayers (the same as the superlattice in Figs. 6 and 7) and one with 12 monolayers. It is evident that the polarization amplitude is inversely proportional to the period of the supercell.

It is these dipole moments in the diatom ionic quadratic response that are responsible for the slight interface asymmetry and macroscopic electric field referred to in the discussion of Fig. 6. Such effects have been studied previously in Refs. 45 (numerically) and 46 (analytically).

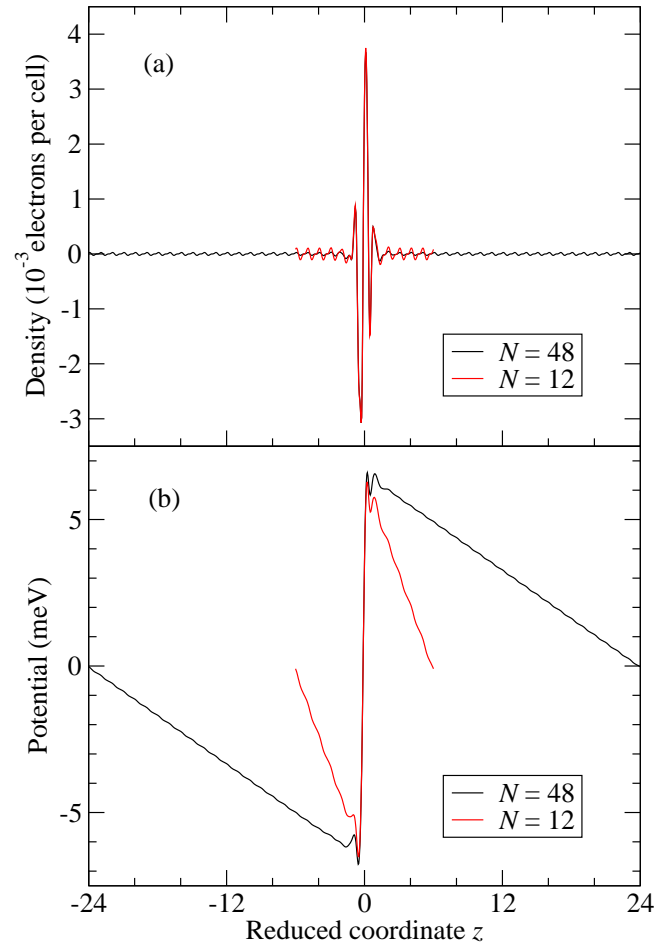


FIG. 10: (Color online) Quadratic response to a diatom ionic perturbation of $\text{In}_{0.765}\text{Ga}_{0.235}\text{As}_{0.5}\text{P}_{0.5}$: (a) electron density, (b) Hartree potential. The perturbations are applied at $z = -0.5$ (As) and $z = +0.5$ (Ga). Results are given for supercells with periods $N = 48$ and $N = 12$.

C. Multipole moments

In Ref. 1, long-wavelength approximations for the density and potential response are developed using power series expansions of $n(k + G)$ and $v(k + G)$ with respect to k , where G is a reciprocal-lattice vector. The expansion coefficients can be found numerically by several methods. One is a simple polynomial fitting of the discrete fast Fourier transform (FFT). Another is to use analytical manipulations of the FFT to obtain expansion coefficients in the form of multipole moments.

In a superlattice, the allowed values of $k + G$ satisfy $k = k\hat{z}$ for small $k\hat{z}$, where \hat{z} is the direction normal to the interface plane. Hence

$$n(k + G) = \frac{1}{N_F} \sum_x^X n(x) e^{i(k+G)_x} \quad (11a)$$

$$= \sum_{l=0}^X (-ik)^l n_l(G); \quad (11b)$$

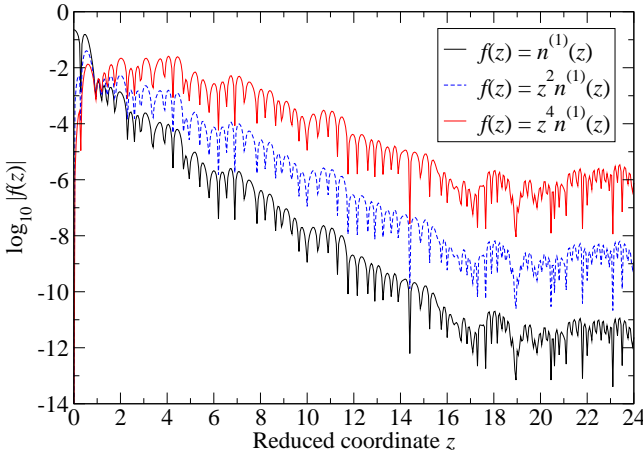


FIG. 11: (Color online) Log-scale plot of linear density response in Fig. 8(a).

where x is a coordinate on the FFT grid, N_F is the number of such points, and the expansion coefficients are

$$n_1(G) = \frac{1}{1!N_F} \sum_x z^1 n(x) e^{iG \cdot x} \quad (12a)$$

$$= \frac{1}{1!} \sum_k [z^1(k, G)] n(k); \quad (12b)$$

where $z^1(k)$ is the FFT of z^1 . The coefficient $n_1(G)$ is, to within a factor of $1!$, just the multipole moment^{38,41} of order 2^1 of the function $n(x) e^{iG \cdot x}$.

Since the FFT grid is finite, the multipole moment $n_1(G)$ always has a well-defined value. Nevertheless, if the response $n(x)$ is not well localized, the value of $n_1(G)$, although finite, does not converge to a meaningful value in the limit of large supercells. It is therefore necessary to check in each case whether the localization is sufficient to use Eq. (12) for the desired values of l .

This is done in Fig. 11 for the linear density response of $A_{10.5}G_{a_{0.5}A_s}$ in the cases $l=0, 2$, and 4 . The response is quasi-exponentially localized over nearly 10 orders of magnitude, to a distance of about 17 monolayers from the perturbation. At this point it attenuates due to the nonanalyticity of the potential-energy smoothing function in Fig. 1. If the potential energy is not smoothed, the quasi-exponential localization extends for another order of magnitude, at which point numerical error takes over. However, the localization obtained here is clearly sufficient to calculate accurate values of the linear quadrupole and hexadecapole moments.

On the other hand, if the plane-wave cutoff in the kinetic energy is not smoothed, $z^4 n^{(1)}(z)$ is not adequately localized, and the hexadecapole moment ($l=4$) has a nonsensical value for the supercell considered here. It is interesting that in this case the result obtained from polynomial fitting does eventually converge to the value given by Eq. (12), but only after several hundred terms are included in the polynomial. By contrast, for the localized functions shown here, the multipole moments are

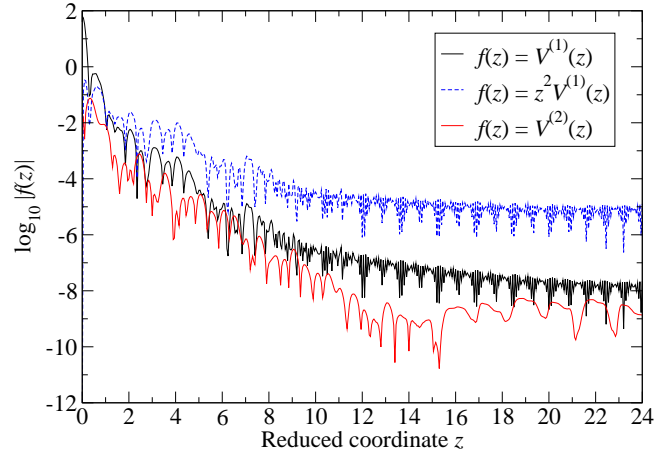


FIG. 12: (Color online) Log-scale plot of linear and quadratic pseudopotential plus exchange-correlation potential for a monolayer in G a perturbation of $A_{10.5}G_{a_{0.5}A_s}$.

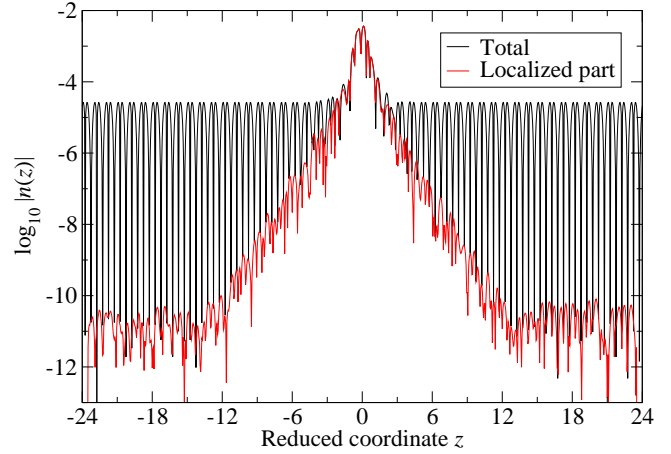


FIG. 13: (Color online) Log-scale plot of the diatom density response in Fig. 10(a). Both the total density and its localized part (excluding the periodic part) are shown.

very close to the values obtained from even the lowest-order polynomials.

The linear and quadratic terms in those parts of the local potential response that are expected to be localized (i.e., the ionic pseudopotential and the exchange-correlation potential) are shown in Fig. 12. Here the features seen in the linear response for $|z| > 10$ are the remnants of Gibbs oscillations in the local ionic pseudopotential that remain even after smoothing of the plane-wave cutoff. (These Gibbs oscillations are not seen in the quadratic response because the ionic pseudopotential is purely linear.) The localization here is not quite as good as for the density, but it is still sufficient to calculate the desired multipole moments.

The log-scale plot in Fig. 13 of the quadratic density response for C_{2v} diatom density perturbations has additional features of interest. The response is not well localized, but this is due to the periodic oscillations shown in Fig.

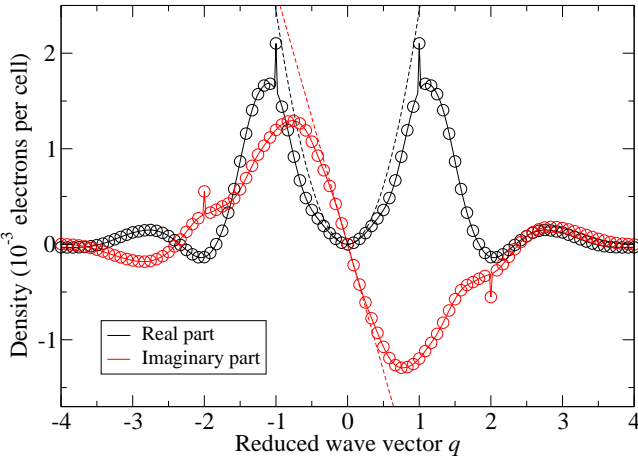


FIG. 14: (Color online) Fourier transform of the diatom-ic density response in Fig. 10(a). Solid lines are for a supercell with $N = 48$ monolayers, while circles are for $N = 12$. The FFT is scaled by N so that the results are comparable. Dashed lines are quadratic (real) and linear (imaginary) polynomials corresponding to the calculated quadrupole and dipole moments.

10. The periodic part can be separated from the rest by evaluating it in the unit cell farthest from the origin. Subtracting the periodic part from the total leaves a remainder that should be localized. This is confirmed in Fig. 13, which shows both the total quadratic response and the localized remainder.

The localized part of the diatom-ic response can be used to obtain multipole moments as above. The periodic part is even simpler, because it merely modulates the values of coefficients in the bulk Hamiltonian.

The results obtained from the calculated density multipole moments $n_1(G = 0)$ are shown in Figs. 8(b) and 14. The power series expansions for the density response are clearly valid only for small wave vectors. For the C_{2v} perturbation in Fig. 14, the reduced symmetry generates a nonvanishing imaginary part in the FFT. This part has a nonzero slope at the origin, leading to the dipole moment observed previously in Fig. 10. There are also noticeable spikes in the FFT at nonzero reciprocal-lattice vectors. These correspond to the periodic part of the response discussed above.

Based on the perturbation scheme developed in Refs. 1 and 46, the following procedure was used to determine the expansion coefficients (12) for the density and potential. In the linear response, for $G \neq 0$, the density and localized potential were both expanded to order $l = 2$. The power series expansion of the Hartree potential (2) was then used to generate the following corrections that were

added to the localized potential coefficients:

$$v_0(G) = \frac{4}{G^2} n_0(G); \quad (13a)$$

$$v_1(G) = \frac{4}{G^2} n_1(G) - \frac{i2G_z}{G^2} n_0(G); \quad (13b)$$

$$v_2(G) = \frac{4}{G^2} n_2(G) - \frac{i2G_z}{G^2} n_1(G) + \frac{1}{G^2} \frac{4G_z^2}{G^4} n_0(G); \quad (13c)$$

On the other hand, for $G = 0$, expanding the potential to order $l = 2$ requires n_1 values up to $l = 4$. The Hartree correction terms for $l = 0, 1, 2$ are then simply

$$v_1(0) = -4 n_{4+2}(0); \quad (14)$$

Finally, in addition to the $l = 0, 1, 2$ power series for the local linear potential, one must include separately the nonanalytic quadrupole contribution $4 n_2(0)_{\text{quad}}$ arising from the q_0 term in Eq. (2). This term merely contributes an overall constant shift in potential. (The nonanalytic monopole term is zero for the isovalent perturbations considered here, while the linear dipole term vanishes for perturbations with T_d or D_{2d} symmetry.)

For the quadratic response, the potential was expanded only to order $l = 0$. For $G \neq 0$, the Hartree correction (13a) was added to the localized potential coefficient, but for $G = 0$, the $l = 0$ correction of the form (14) was not added to the localized potential. Instead, the entire dipole and quadrupole Hartree terms for $G = 0$ were treated as separate nonanalytic contributions.

D. Error in the linear and quadratic approximations

To test the validity of truncating the power series in the nonlinear response (7), the effects of various truncations were examined by comparing them with the exact superlattice density and potential given previously in Figs. 4 and 6. The approximations are generally good enough that they are difficult to distinguish visually from the exact results. Therefore, only the error in the approximations is plotted here.

The results for the GaAs/AlAs superlattice are shown in Fig. 15. Part (a) shows the error when the superlattice density is approximated by the periodic reference crystal density, comparing it with the error in the linear and quadratic approximations. The latter are both small on the scale of the reference crystal error (which is itself small on the scale of the reference density), so the linear and quadratic errors are plotted on an expanded scale in part (b). The corresponding errors in the Hartree potential are shown in part (c). It can be seen that the quadratic approximation is quite accurate, with an error of only about 2 meV.

The errors in the linear and quadratic approximations for the $\text{In}_{0.53}\text{Ga}_{0.47}\text{As}/\text{InP}$ superlattice are shown in Fig.

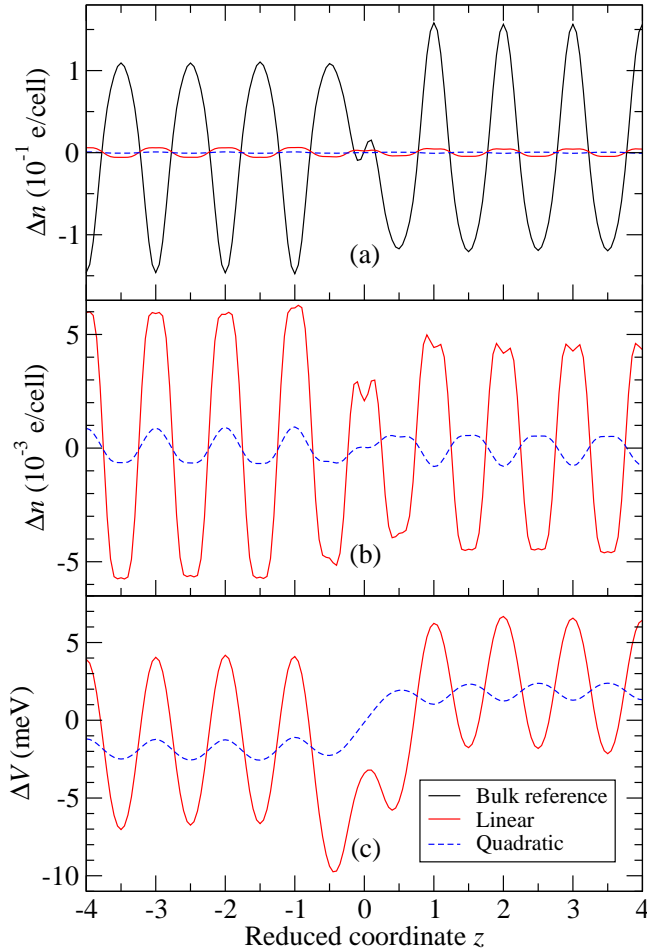


FIG. 15: (Color online) Errors in the electron density and Hartree potential of a GaAs/AlAs superlattice under various approximations: (a) Errors in the reference crystal density and the densities obtained in the linear and quadratic approximations. (b) Expanded view of the linear and quadratic errors in (a). (c) Errors in the linear and quadratic approximations to the Hartree potential.

16. Again, the error in the quadratic Hartree potential is limited to about 2 meV.

Using multipole expansions for the density and potential introduces an additional source of error. To illustrate this, Fig. 17 shows the electron density and Hartree potential in coordinate space calculated directly from the FFT of the truncated multipole expansion (with 0 1 4 for the linear density and 0 1 2 for the quadratic density). Note that the scale of this figure is much larger than any of the others. In fact, in a continuous coordinate space, these quantities would be derivatives of Dirac functions. Clearly these multipole expansions yield a very poor approximation of the original density and potential.

However, in an envelope-function model, accuracy is only required at small wave vectors, so it is more appropriate to compare the macroscopic average⁴⁰ of the multipole expansions with the macroscopic average of the

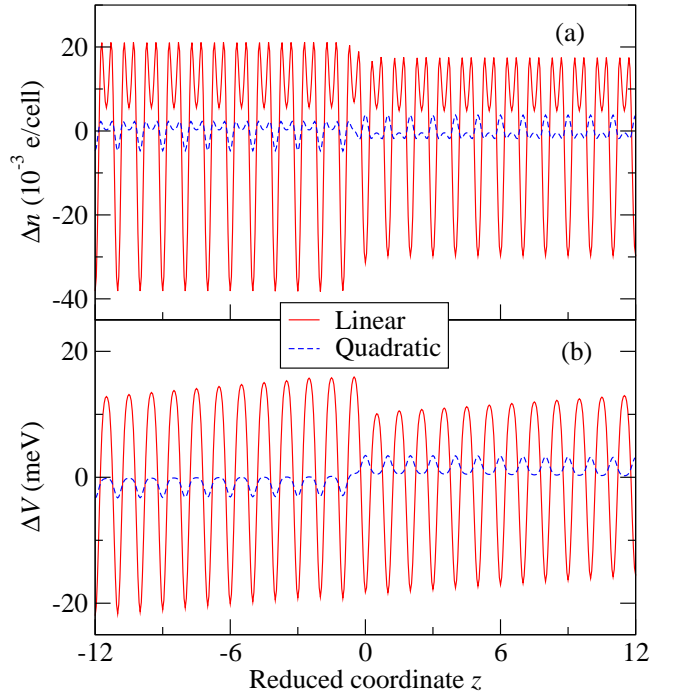


FIG. 16: (Color online) Errors in the electron density and Hartree potential of an $In_{0.53}Ga_{0.47}As/InP$ superlattice under various approximations: (a) Errors in the linear and quadratic densities. (b) Errors in the linear and quadratic Hartree potentials.

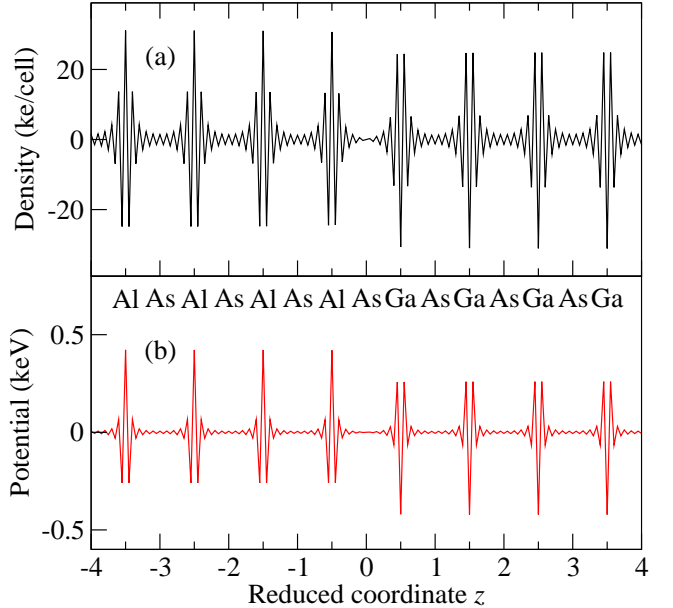


FIG. 17: (Color online) Sum of the linear and quadratic perturbations for (a) the electron density and (b) the Hartree potential constructed from quadrupole and hexadecapole moments in a GaAs/AlAs superlattice. The perturbations are finite only because a discrete coordinate grid is used. The hexadecapole terms are dominant here, although this is no longer true after macroscopic averaging.

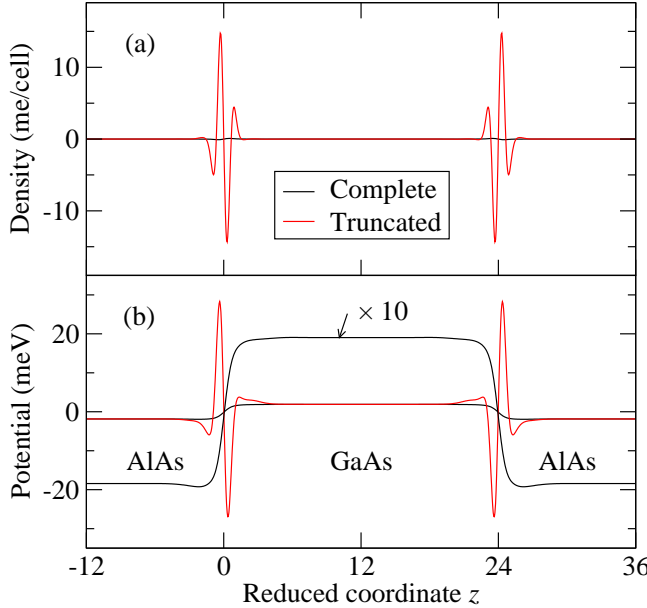


FIG. 18: (Color online) Errors in the macroscopic (a) electron density and (b) Hartree potential of a GaAs/AlAs superlattice under various approximations. The functions shown are the errors in the complete quadratic approximation to the macroscopic density and potential (i.e., the macroscopic averages of the quadratic functions in Fig. 15) and the corresponding errors when the linear and quadratic responses are generated from truncated multipole expansions. The substantially larger error in the truncated results is caused mainly by the neglect of all terms beyond the hexadecapole moment in the linear density response [see Fig. 8(b)].

exact results. This is done in Fig. 18, which shows the errors in the macroscopic density and Hartree potential for a GaAs/AlAs superlattice. The macroscopic errors are virtually identical in bulk, but the truncated multipole approximation introduces a significant additional error in a narrow region near the interfaces. This arises primarily from the neglect of terms with $l \geq 6$ in the linear response. Note that the peak value of the macroscopic error has no absolute meaning, because it can be reduced with a different choice of averaging function. Due to the narrowness of the region where the error is nonzero, it is not expected to have a large effect on slowly varying envelope functions.

The corresponding results for $\text{In}_{0.53}\text{Ga}_{0.47}\text{As}/\text{InP}$ are shown in Fig. 19. Again, the additional error generated by the truncation of the multipole series vanishes outside a narrow region near the interfaces. The magnitude of the error is similar to that in GaAs/AlAs. For $\text{In}_{0.53}\text{Ga}_{0.47}\text{As}/\text{InP}$, however, there is a slight error in the bulk macroscopic electric fields even before the multipole expansion is truncated.

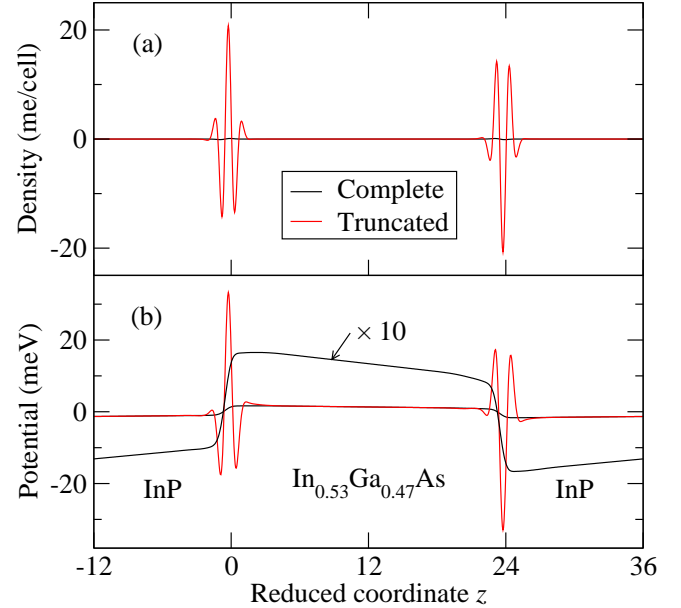


FIG. 19: (Color online) Errors in the macroscopic (a) electron density and (b) Hartree potential of an $\text{InP}/\text{In}_{0.53}\text{Ga}_{0.47}\text{As}$ superlattice: comparison of the complete quadratic errors with the truncated multipole errors, as in Fig. 18.

E. Nonlocal pseudopotential

The nonlocal part of the pseudopotential was handled by polynomial fitting in k space. For the bulk reference crystal, the entire plane-wave Hamiltonian matrix $H(k+G_i; k+G^0) = H_{G^0}(k)$ was evaluated at 57 points near $k = 0$, including $k = 0$ itself and points of the form $h100i, h110i, h111i, h200i$, and $h210i$, where h is some specified interval (usually set equal to the magnitude of the smallest superlattice reciprocal-lattice vector). It is important to choose a set of fitting points with O_h symmetry so that the fitted coefficients maintain the T_d symmetry and time-reversal symmetry of the Hamiltonian. The Hamiltonian was fitted to a general polynomial of order k^4 with 35 independent coefficients. (For general G and G^0 , there is no special symmetry that can be used to reduce the number of coefficients.)

For the linear response, the nonlocal pseudopotential $V^{nl}(k+g; k+g^0)$ may be written as $V_{GG^0}^{nl}(k_x; k_y; k_z + \frac{1}{2}(g_z + g_z^0))$, $g_z = g_z^0$, in which g is a reciprocal-lattice vector of the superlattice and $g = g/G$ is an integer multiple of $(2\pi N d)\hat{z}$, where N is the number of monolayers in the superlattice and $d = \frac{1}{2}a$ is the monolayer spacing. The function $V_{GG^0}^{nl}(k_1; k_2; k_3; k_4)$ was fitted to a general polynomial of order k^2 with 15 independent coefficients using a set of 33 points arranged on a cubic grid. A larger grid was tested using fitting polynomials of order k^4 , but the difference was negligible so only the simpler method was used. The nonlocal pseudopotential is purely linear, so no fitting of the quadratic response was necessary.

IV. ENVELOPE-FUNCTION HAMILTONIAN

The next step is to use the k -space expansion coefficients for the quadratic density and short-range potentials to construct an envelope-function Hamitonian. The entire set of expansion coefficients including the local and nonlocal potentials was subjected to the unitary transformation given in Eq. (4.15) of Ref. 1, which converts all matrices from the plane-wave basis to a Luttinger-Kohn basis of zone-center Bloch functions for the reference crystal. Perturbation theory was then used to reduce these 283 × 283 matrices to a much smaller dimension by eliminating the coupling between states in the set A of interest (e.g., $A = f_{15v}g$) and all other states. The Luttinger-Kohn unitary transformation method^{2,5,13,14,47} was used in order to obtain energy-independent Hamitonian parameters. The basic perturbation formulas are summarized in Appendix A.

The renormalized Hamitonian for set A in the reference crystal is defined by its matrix elements (in the Luttinger-Kohn basis)

$$\hbar k \mathbf{H}^{(0)} \mathbf{j}^0 \mathbf{k}^0 i = \langle \mathbf{E}_n | \mathbf{n}^0 | \mathbf{k}^0 \rangle + k_i \mathbf{n}^0 \mathbf{k}^0 + k_i k_j D_{nn^0}^{ij} + k_i k_j k_l C_{nn^0}^{ijl} + k_i k_j k_l k_m Q_{nn^0}^{ijlm} \rangle_{kk^0}; \quad (15)$$

the coefficients of which are defined in Appendix B. Since the set $A = f_{15v}g$ will be the focus of subsequent numerical study, symmetry restrictions on the kinetic momentum matrix \mathbf{n}^0 and the inverse effective-mass tensor $D_{nn^0}^{ij}$ are of interest. From the symmetry of the zinc-blende crystal, the matrix \mathbf{n}^0 must have the form

$$\mathbf{n}^0 = iR \mathbf{j}_{ijk} \mathbf{f} \mathbf{I}_j \mathbf{I}_k \mathbf{g}; \quad (16)$$

where \mathbf{j}_{ijk} is the antisymmetric unit tensor, $fABg = \frac{1}{2}(AB + BA)$, and \mathbf{I}_j is the j component of the orbital-angular momentum in a basis $A = f_X i; f_Y j; f_Z k$ of p -like orbitals.⁴⁸ The coefficient $R = i_{xy}^z$ is real by time-reversal symmetry, and the hermiticity of the Hamitonian requires $R = R = 0$. Likewise, the $D_{nn^0}^{ij}$ matrix is given by⁴⁸

$$D_{nn^0}^{ij} = L_{ij} \mathbf{1} + M_{ij} \mathbf{I}_i^2 + N_{ij} (1 - \mathbf{I}_i^2) f \mathbf{I}_i \mathbf{I}_j \mathbf{g} + \frac{1}{2} K_{ijk} \mathbf{I}_j \mathbf{I}_k; \quad (17)$$

where $\mathbf{1}$ represents the 3×3 unit matrix and the constants $L = D_{xx}^{xx}$, $M = D_{xy}^{yy}$, $N = D_{xy}^{xy} + D_{xy}^{yx}$, and $K = D_{xy}^{xy} - D_{xy}^{yx}$ are real. Here L , M , and N determine the anisotropic f_{15v} effective masses, while K is the effective Lande g factor for the valence band.⁴⁸

The renormalized linear-response Hamitonian for set A is given by¹

$$\hbar k \mathbf{H}^{(1)} \mathbf{j}^0 \mathbf{k}^0 i = \langle \mathbf{k}^0 | \mathbf{k}^0 \rangle H_{nn^0}(\mathbf{k}; \mathbf{k}^0); \quad (18)$$

where $\langle \mathbf{k}^0 | \mathbf{k}^0 \rangle$ is the Fourier transform¹ of the atomic dis-

tribution function \mathbf{R} and

$$H_{nn^0}(\mathbf{k}; \mathbf{k}^0) = E_{nn^0} + \mathbf{n}^0 \mathbf{k}^0 + k_i \mathbf{n}^0 \mathbf{k}^0 + \mathbf{n}^0 \mathbf{k}^0 + k_i k_j D_{nn^0}^{ij} + k_i D_{nn^0}^{ij} k_j^0 + D_{nn^0}^{ij} k_i k_j^0; \quad (19)$$

Here $E_{nn^0} = 4 n_2(0)$ is the nonanalytic contribution⁴⁹ from the linear quadrupole moment of the electron density, which merely shifts the mean energy by a constant; the remaining terms are defined in Appendix C. The notation has been modified with respect to Ref. 1 in order to draw attention to similarities with the bulk Hamitonian (15) and avoid undue proliferation of symbols. It should be noted that the superscripts on the coefficients in Eq. (19) indicate how the coordinate and momentum operators are ordered; for example, in the coordinate representation, the term proportional to $D_{nn^0}^{ij}$ has the form $D_{nn^0}^{ij} p_i(x) p_j$, where p is the momentum operator.

The symmetry of the coefficients in Eq. (19) is the same as the symmetry of site in the reference crystal. For a zinc-blende reference crystal, the atomic sites have the same point group T_d as the reference crystal, but in nonsymmetric crystals (e.g., diamond) the site symmetry is lower than the crystal symmetry.⁵ Thus, the linear momentum matrix for $A = f_{15v}g$ has the same form as in bulk:

$$\mathbf{n}^0 = iR \mathbf{j}_{ijk} \mathbf{f} \mathbf{I}_j \mathbf{I}_k \mathbf{g}; \quad (20a)$$

$$\mathbf{n}^0 = iR \mathbf{j}_{ijk} \mathbf{f} \mathbf{I}_j \mathbf{I}_k \mathbf{g}; \quad (20b)$$

where the superscript dots are just placeholders to indicate where p is positioned with respect to (x) . As in the bulk case, $R = i_{xy}^z$ and $R = i_{xz}^y$ are real by time-reversal symmetry; however, for the linear response, hermiticity [i.e., $\mathbf{n}^0 = (\mathbf{n}^0)^*$] requires only that $R = R$. Therefore, unlike the bulk case, the linear R coefficients are not required to vanish. As discussed in Ref. 1 (using a different notation), the constant R generates a δ -function-like mixing of the f_{15v} and f_{15g} valence states at a (001) heterojunction.⁵⁰ This mixing is considered in greater detail below.

The linear D tensor likewise has the same form as in bulk material:

$$D_{nn^0}^{ij} = L_{ij} \mathbf{1} + M_{ij} \mathbf{I}_i^2 + N_{ij} (1 - \mathbf{I}_i^2) f \mathbf{I}_i \mathbf{I}_j \mathbf{g} + \frac{1}{2} K_{ijk} \mathbf{I}_j \mathbf{I}_k; \quad (21)$$

with similar definitions for $D_{nn^0}^{ij}$ and $D_{nn^0}^{ij}$. All of the coefficients L , etc., are real by time-reversal symmetry. Hermiticity of the Hamitonian requires that $D_{nn^0}^{ij} = (D_{nn^0}^{ji})^*$ and $D_{nn^0}^{ij} = (D_{nn^0}^{ji})^*$, which yields constraints of the form $K_{ijk} = K_{ijk}$, etc., but does not require any of the constants in (21) to be zero.

As discussed in the Introduction, for any heterostructures the energy gap is not very large in comparison to the band offsets, which means that the linear approximation for the momentum and mass terms used in Ref. 1 is not very accurate in a single-band model. In an effort

to learn more about the limits of single-band models, the perturbative renormalization of them momentum and mass terms was extended to terms quadratic in k , with the results given in Appendix D. The resulting contributions can be written in the form

$$\hbar k_j H^{(2)} j^0 k^0 i = \begin{matrix} X & 0X \\ & k^0 \end{matrix} (k^0 \quad k^0 \quad k^0 \quad k^0) \\ ; \quad k^0 \\ H_{nn^0}(k; k^0; k^0); \quad (22)$$

in which

$$H_{nn^0}(k; k^0; k^0) = E_{nn^0} + k_i \begin{matrix} i \\ nn^0 \end{matrix} + k_i^0 \begin{matrix} i \\ nn^0 \end{matrix} + \begin{matrix} i \\ nn^0 \end{matrix} k_i^0 \\ + k_i k_j D_{nn^0}^{ij} + k_i D_{nn^0}^{ij} k_j^0 + D_{nn^0}^{ij} k_i^0 k_j^0 \\ + k_i k_j^0 D_{nn^0}^{ij} + k_i^0 D_{nn^0}^{ij} k_j^0 + D_{nn^0}^{ij} k_i^0 k_j^0; \quad (23)$$

Here again the superscripts indicate the positioning of the associated operators, with (for example) the term proportional to $\begin{matrix} i \\ nn^0 \end{matrix}$ having the form $\begin{matrix} i \\ nn^0 \end{matrix}(x)p_i(x)$ in coordinate space. Hermiticity of the Hamiltonian gives constraints such as $D_{nn^0}^{ij} = D_{nn^0}^{ji}$. It should be noted that Eqs. (22) and (23) include only those quadratic contributions arising from perturbative renormalization; the other terms arising from direct multipole expansions of the quadratic response have a different form and are considered in Appendix E.

For the ^{15}V Hamiltonian, the coefficients in Eq. (23) also have T_d symmetry, so they are given by obvious generalizations of Eqs. (20) and (21). The hermiticity constraints on the R coefficients are $R^2 = R$ and $R^3 = R$ (which implies that $R^0 = 0$), and one can also choose these coefficients to satisfy $R^2 = R^3$ because R^2 and R^3 commute. Likewise, the D coefficients L, M, N , and K all satisfy constraints of the form $K^2 = K^3$, $K^0 = K^1$, $K^1 = K^2$, and $K^0 = K^1$, and one can choose them to satisfy $K^2 = K^3$ too.

In a (001) heterostructure, where $(x) = (z)$, the bulk Hamiltonian matrix elements of the form Lp_z^2 and Mp_z^2 are replaced (to order 2) by

$$Lp_z^2 = L^{(0)}p_z^2 + L(p_z^2 + p_z^2) + Lp_zp_z \\ + L(p_z^2 + p_z^2) + Lp_zp_z \\ + L(p_zp_z + p_zp_z) + Lp_z^2; \quad (24)$$

where summation on i and j is implicit. This is a linear combination of all but one of the von Roos operators¹⁶ defined in Eq. (1). If the renormalization were extended to cubic order, we would find also a term

$$L(p_zp_z + p_zp_z); \quad (25)$$

Hence, the present derivation from perturbation theory supports not a single operator having the form (1) with fixed exponents, but a linear combination of all possible operator orderings. As mentioned in the Introduction, this does not lead to any mathematical or physical

difficulties because (x) is a smooth function of x . The question of whether any particular term is in the linear combination might happen to be negligible is considered in Sec. V.

In a similar fashion, bulk matrix elements of the form Np_xp_z are replaced in a (001) heterostructure by

$$Np_xp_z = N^{(0)}p_xp_z + (N^0 + 2N^1)p_xfp_z; \quad g \\ + (N^1 + N^2) + 2N^2)p_xfp_z; \quad g \\ + (N^2 + N^3)p_xp_z; \quad (26)$$

where $N^f = \frac{1}{2}(N^0 + N^1)$. Note that the final term proportional to p_z is not found in the usual symmetrization recipe for envelope-function Hamiltonians.^{51,52}

In a (001) heterostructure, the contribution of the R terms to the Hamiltonian is

$$H_R = i2f_IxI_yg(R[p_z; \quad] + R[p_z; \quad] \\ + R[p_z; \quad]); \quad (27)$$

which fixes the j and j' valence states because

$$2 \quad \begin{matrix} 3 \\ 0 \quad 1 \quad 0 \end{matrix} \\ 2f_IxI_yg = 4 \quad \begin{matrix} 1 \quad 0 \quad 05 \\ 0 \quad 0 \quad 0 \end{matrix}; \quad (28)$$

The function (z) is a smooth step-like function, hence $i[p_z; \quad] = d/dz$ is localized at interfaces and has the form of a macroscopic average of the Dirac function. The function $[p_z; \quad]$ is also localized, but the associated term in (27) cannot be written as a simple derivative because $R^2 = R$. Mixing of the type (27) has been studied by Ivchenko et al.⁵⁰

The contribution of the K terms in a (001) heterostructure is very similar:

$$H_K = \frac{i}{2}(p_xI_y - p_yI_x)K[p_z; \quad] \\ + (K^0 + K^1) + (K^2 + K^3)p_z; \quad (29)$$

Here the operator $(p_xI_y - p_yI_x)$ is analogous to the Rashba coupling^{14,53,54} $(p_x - p_y)$ in the conduction band, so contributions of the form (29) have been referred to as the valence-band Rashba coupling.^{47,55,56} As discussed in Ref. 1, this type of coupling was introduced in Ref. 57 under an approximation that is equivalent to assuming that the Rashba coefficient is the same as the effective Lande factor K in bulk material. This has the advantage of reducing the number of unknown parameters, since K is known from magnetoabsorption experiments (see, e.g., Ref. 58). However, the bulk Lande factor to order 2 is given by

$$K = K^{(0)} + K^1 + K^2; \quad (30a)$$

TABLE I: Luttinger parameters for several bulk compounds and their virtual-crystal averages.

	GaAs	Al _{0.5} Ga _{0.5} As	AlAs
L	5.028	3.648	2.863
M	1.511	1.326	1.126
N	6.146	4.676	3.792
K	2.086	0.993	0.514
	In _{0.53} Ga _{0.47} As	In _{0.765} Ga _{0.235} As _{0.5} P _{0.5}	InP
L	5.596	4.187	3.317
M	1.385	1.253	1.119
N	6.590	5.071	4.087
K	2.797	1.609	0.974

where

$$K = K + 2K ; \quad (30b)$$

$$K = K + 2K + K + K + K ; \quad (30c)$$

which shows that the Rashba coupling (29) is generally independent of the bulk Lande factor. To linear order, replacing the Rashba coefficient with K would be a good approximation if $2K \gg K$. As shown in Sec. V, this is true in some materials but not in others; hence, it cannot be presumed to hold true in general.

V. EFFECTIVE-MASS PARAMETERS

In this section, the numerical values of the envelope-function parameters calculated for the model system are examined to see whether any general conclusions can be drawn regarding the structure of the Hamiltonian in Sec. IV. Values of the Luttinger parameters⁴⁸ L, M, N, and K calculated for various bulk materials are listed in Table I. This table shows that the parameters are of order 1 (in atomic units), and that their dependence on material composition is not linear. For example, the change (relative to the reference crystal) in K is about 1 for GaAs but only $\frac{1}{2}$ for AlAs. It should be noted that the bulk K values reported here include only the contributions from $k \cdot p$ renormalization, since the asymmetric term in the nonlocal pseudopotential⁵⁹ cannot be determined by polynomial fitting.⁶⁰

To obtain a measure of the accuracy of the linear and quadratic approximations, the change in effective-mass parameters for various bulk compounds relative to the reference crystal was calculated in these approximations using expressions of the form (30) and compared with the exact changes. The results of these calculations are given in Table II. The top part of the table considers the changes in GaAs and Al_{0.2}Ga_{0.8}As relative to the reference crystal Al_{0.1}Ga_{0.9}As. Here the linear approximation is accurate to better than 10%, while the quadratic approximation is accurate to better than 1%. Since the linear changes are already a small perturbation in this case, the linear approximation for GaAs/Al_{0.2}Ga_{0.8}As should be adequate for most purposes.

Note that M, which determines the mass of heavy holes along the h100 directions, is much more accurate than L, N, and K. This happens because the coupling of $15v$ to $1c$ does not contribute to M,⁶¹ so the remote bands in M are more remote and the heterostructure perturbation for M is "shallower" than for the other parameters. As discussed in the Introduction, one can achieve a similar effect for L, N, and K by including $1c$ in the set A.

For the case of GaAs/AlAs (with Al_{0.5}Ga_{0.5}As as the reference crystal), the linear approximation is off by nearly 50% in some cases, while the quadratic approximation is accurate to within 13% for K and to within 8% for the other parameters. The quadratic approximation is more accurate for In_{0.53}Ga_{0.47}As/InP, with a maximum error of less than 4%. Although these results are not perfect, an accuracy of around 10% in a small perturbation is good enough in many cases, and as shown in Sec. VI, the quadratic approximation for A = f_{15v} yields reasonably good band structures over a limited range of energies (although not as good as for a multi-band Hamiltonian).

Calculated values of various parameters in the $15v$ linear-response Hamiltonian (19) are listed in Table III. The linear changes in the bulk Luttinger parameters are determined by constants L, M, N, and K of the form (30b). As noted below Eq. (29), the linear contribution to the valence-band Rashba coupling is just K.

Many envelope-function calculations in the literature use the BenD aniel-Duke operator ordering^{6,51,52,62,63} in which it is assumed that $\mathcal{J} \mathcal{J} \mathcal{J} \mathcal{J} \mathcal{M} \mathcal{J} \mathcal{M} \mathcal{J}$ and $\mathcal{N} \mathcal{J} \mathcal{J} \mathcal{N} \mathcal{J}$. Inspection of Table III shows that this is perhaps a tolerable approximation in some cases (e.g., light holes in GaAs/AlAs), but it is a bad approximation in others (e.g., heavy holes in GaAs/AlAs). It should be noted that Bastard⁶³ and Burt⁶ both derive the BenD aniel-Duke ordering using variations of Lowdin perturbation theory,⁶⁴ which yields energy-dependent mass parameters. This type of perturbation theory cannot be used to draw conclusions about operator ordering in a Hamiltonian with energy-independent parameters, since Luttinger-Kohn perturbation theory is qualitatively different. A detailed comparison of the two theories is outside the scope of this paper, but it will be noted that a direct application of Lowdin perturbation theory (using a power series expansion to treat the energy dependence of the denominators) to the present first-principles calculations yields values of L, M, and N that are smaller than those in Table III, but still not generally negligible.

As mentioned in Sec. IV, it is also common practice to estimate the Rashba coupling K by the approximation⁵⁷ $K' \approx K$, which amounts to an extension of the BenD aniel-Duke hypothesis to the asymmetric terms in the Luttinger Hamiltonian.⁴⁸ Table III shows that this is a good approximation for cationic perturbations in GaAs/AlAs and In_{0.53}Ga_{0.47}As/InP, but not for anionic perturbations in In_{0.53}Ga_{0.47}As/InP. Hence, as noted in Ref. 1, this approximation can only

TABLE II: Difference between Luttinger parameters of bulk crystals and average reference crystal: Comparison of linear and quadratic approximations with exact differences. Error columns give per cent relative error.

GaAs								Al _{0.2} Ga _{0.8} As			
Linear		Quadratic		Exact		Linear		Quadratic		Exact	
	Value	Error	Value	Error	Value	Error	Value	Error	Value	Exact	Value
L	0.329710	7.22%	0.353495	0.526%	0.355363	0.329710	7.21%	0.305924	0.526%	0.307542	
M	0.035986	0.99%	0.035632	0.003%	0.035634	0.035986	0.98%	0.036339	0.004%	0.036341	
N	0.347108	6.83%	0.370680	0.501%	0.372548	0.347108	6.75%	0.323536	0.498%	0.325154	
K	0.273357	8.70%	0.297525	0.623%	0.299389	0.273357	8.99%	0.249189	0.644%	0.250803	
GaAs								AlAs			
L	0.9968	27.8%	1.2706	7.93%	1.3800	0.9968	27.0%	0.7230	7.85%	0.7846	
M	0.1933	4.5%	0.1855	0.24%	0.1850	0.1933	3.6%	0.2011	0.27%	0.2005	
N	1.0919	25.7%	1.3609	7.43%	1.4701	1.0919	23.5%	0.8229	6.93%	0.8841	
K	0.7004	35.9%	0.9828	10.05%	1.0926	0.7004	45.9%	0.4179	12.92%	0.4799	
In _{0.53} Ga _{0.47} As								InP			
L	1.1067	21.5%	1.3650	3.12%	1.4091	1.1067	27.2%	0.8483	2.53%	0.8703	
M	0.1338	2.1%	0.1319	0.63%	0.1311	0.1338	0.6%	0.1358	0.77%	0.1347	
N	1.2192	19.7%	1.4758	2.84%	1.5189	1.2192	24.0%	0.9626	2.13%	0.9835	
K	0.8778	26.1%	1.1431	3.77%	1.1879	0.8778	38.1%	0.6125	3.63%	0.6355	

TABLE III: Linear parameters in the ^{15}V Hamiltonian. Here RC stands for reference crystal, and the labels light and heavy holes refer to the bulk properties in the $\text{h}100\text{i}$ directions.

RC	Al _{0.5} Ga _{0.5} As		In _{0.765} Ga _{0.235} As _{0.5} P _{0.5}	
	Ga	As	Ga	As
Light hole	L	1.984	1.806	0.847
	L	1.341	0.586	1.002
	L	0.321	0.610	+ 0.077
Heavy hole	M	0.387	0.329	+ 0.130
	M	0.039	0.109	+ 0.093
	M	0.174	0.110	+ 0.018
k^2 mixing	N	2.181	2.074	0.771
	N	1.542	0.550	1.085
	N	0.320	0.762	+ 0.157
Lande	K	1.399	1.287	0.993
Rashba	K	1.372	0.464	1.089
	K	0.013	0.411	+ 0.048
mixing	R	0.028	0.017	0.038

be relied on in general to produce a rough order-of-magnitude estimate of the Rashba parameter K .

Numerical values for the quadratic renormalization terms in Eq. (23) are listed in Table IV. The bulk values in this table are defined by expressions of the form (30c). It should be noted that the present calculations on (001) supercells do not provide separate values for the constants N^f , N^g , and N^h , since these terms always appear together in the sums $N^f + N^g$ and $N^h + N^f$ (the same is true for K). Table IV is not discussed here beyond a brief comment that, although BENDaniel-Duke operator ordering is not a very good approximation in any case, it is typically better for light holes than for heavy holes, and better for cation perturbations than for anion perturbations. Of course, since the position-dependent corrections to the bulk value of M are rather small, heavy-hole calculations are also less

TABLE IV: Quadratic parameters in the ^{15}V Hamiltonian. Here $N^f = N^h + N^g$, $N^g = N^h + N^f$, $N^f = \frac{1}{2}(N^h + N^g)$, and $N^{[1]} = N^h - N^f$, with similar definitions for K .

RC	Al _{0.5} Ga _{0.5} As		In _{0.765} Ga _{0.235} As _{0.5} P _{0.5}		
	(;)	(Ga;Ga)	(As;As)	(Ga;Ga)	(As;Ga)
L	1.087	0.633	0.668	0.262	
L	0.718	0.640	1.118	0.111	
L	+ 0.051	+ 0.164	+ 0.190	+ 0.026	
L	0.007	0.081	0.002	+ 0.010	
L	0.232	0.120	+ 0.036	0.235	
L	0.232	0.120	+ 0.036	+ 0.020	
M	+ 0.0310	+ 0.0014	0.0265	+ 0.0129	
M	0.0040	0.0119	0.1111	+ 0.0009	
M	+ 0.0301	+ 0.0209	+ 0.0463	+ 0.0065	
M	0.0004	0.0077	+ 0.0018	+ 0.0050	
M	0.0124	0.0104	0.0050	0.0066	
M	0.0124	0.0104	0.0050	+ 0.0007	
N	1.074	0.638	0.679	0.252	
N	0.965	0.787	1.195	0.225	
N	+ 0.069	+ 0.183	+ 0.243	+ 0.035	
N	0.248	0.216	+ 0.031	0.097	
N ^[1]	0.0	0.0	0.0	0.271	
K	1.128	0.660	0.629	0.278	
K	0.933	0.746	0.966	0.217	
K	+ 0.009	+ 0.133	+ 0.151	+ 0.019	
K ^[1]	0.213	0.180	+ 0.035	0.099	
K ^[1]	0.0	0.0	0.0	0.248	
R	0.0076	+ 0.0034	0.0185	0.0034	
R	0.0	0.0	0.0	0.0048	

sensitive to the choice of operator ordering.)

Finally, it should be emphasized that the numbers reported here are not expected to be accurate. They are merely intended to provide a crude picture of some of the qualitative features that would be found in a more

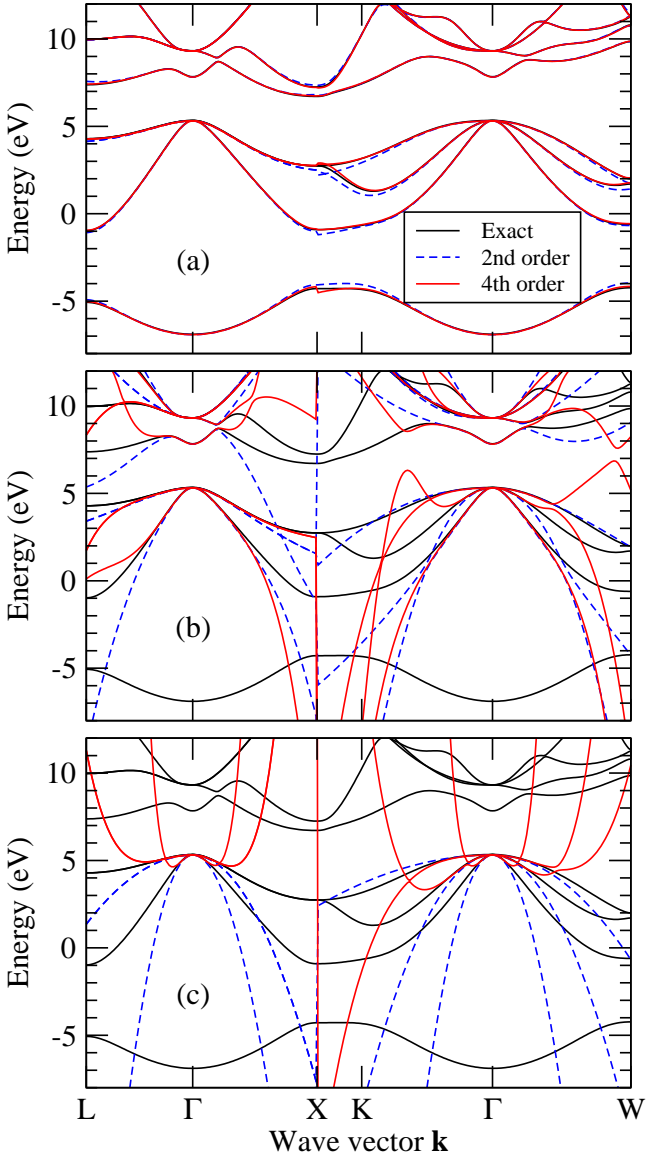


FIG. 20: (Color online) Energy band structure of bulk $\text{Al}_{0.5}\text{Ga}_{0.5}\text{As}$: comparison of exact calculation with $O(k^2)$ and $O(k^4)$ k - p models. (a) 283-state k - p model; (b) 7-state k - p model; (c) 3-state k - p model.

accurate quasiparticle calculation.

V I. SUPERLATTICE VALENCE SUBBAND STRUCTURE

In this section, "exact" model calculations of the valence subband structure of (001) superlattices are used to evaluate the accuracy of various approximate envelope-function models. As a starting point, the bulk band structure of $\text{Al}_{0.5}\text{Ga}_{0.5}\text{As}$ (used as a reference crystal for GaAs/AlAs) is considered in Fig. 20. Part (a) shows the results when all 283 states of the plane-wave basis are retained in the k - p Hamiltonian. Here it makes little

difference whether the polynomials in the k - p Hamiltonian are terminated at order k^2 or k^4 ; both cases provide a good description throughout the Brillouin zone. In part (b), the set $A = f_{15c}, 1c, 15v$ contains 7 states (or 14 with spin^{65,66}). The description of the band structure is still accurate near Γ , although spurious solutions within the energy gap do occur for both the $O(k^2)$ and $O(k^4)$ k - p models.

Part (c) gives the results for $A = f_{15v}$. Here there are no spurious solutions in the $O(k^2)$ effective-mass model, but the spurious solutions for the $O(k^4)$ model occur at rather small wave vectors. The critical point at which the light-hole band has zero slope is about $\frac{1}{6}$ of the distance to the X point. To prevent problems with spurious solutions, the envelope functions in a (001) superlattice should contain no Fourier components beyond this point.⁶⁷ Therefore, a superlattice with a period of 48 monolayers was chosen as the standard test case, since this permits the inclusion of 9 envelope-function plane waves within the region $k_z j \frac{4}{48} (4 = a) = \frac{1}{6} (2 = a)$. Previous calculations on empirical pseudopotential models show that this is sufficient to achieve reasonably accurate results.^{8,9,10,11}

The features shown in Fig. 20(c) have a direct analog in the Dirac equation for relativistic electrons, for which the dispersion relation is

$$E = \frac{p}{p^2 c^2 + m^2 c^4} \quad (31a)$$

$$= m c^2 + \frac{p^2}{2m} - \frac{p^4}{8m^3 c^2} + \quad : \quad (31b)$$

Here the power series converges only when $p c < m c$. If the series is terminated at order p^4 , the slope of $E(p)$ changes sign at $p = \frac{p}{2m} c$, which lies outside the region of validity of the power series. Although the convergence radius of Luttinger-Kohn perturbation theory for the k - p Hamiltonian is not known, one would expect it also to be of the same order of magnitude as the critical point where $E(k)$ changes sign. Therefore, it is reasonable to choose this as the cut-off for plane-wave expansions,⁶⁷ even though it may lie slightly outside the convergence radius of the perturbation power series.

The $\text{GaAs/Al}_{0.2}\text{Ga}_{0.8}\text{As}$ material system historically provided one of the first direct comparisons between experiment and effective-mass theory in heterostructures.⁶⁸ Figure 21 shows the top 12 valence subbands in a (001) $(\text{GaAs})_{24}(\text{Al}_{0.2}\text{Ga}_{0.8}\text{As})_{24}$ superlattice. The exact model calculations are compared here with a 3-state $15v$ envelope-function model based on the theory of Ref. 1, in which terms of order k^3 and k^4 are included only for the bulk reference crystal, the mass and momentum terms are linear in k , and the potential is quadratic in k . The envelope-function results are in excellent agreement with the exact calculations; the mean error in each of the first 10 subbands does not exceed 0.1 meV. Note that the valence-band offset in this system is only 104 meV, which means that the heterostructure perturbation is indeed shallow³ even in a single-band $15v$ model. These results

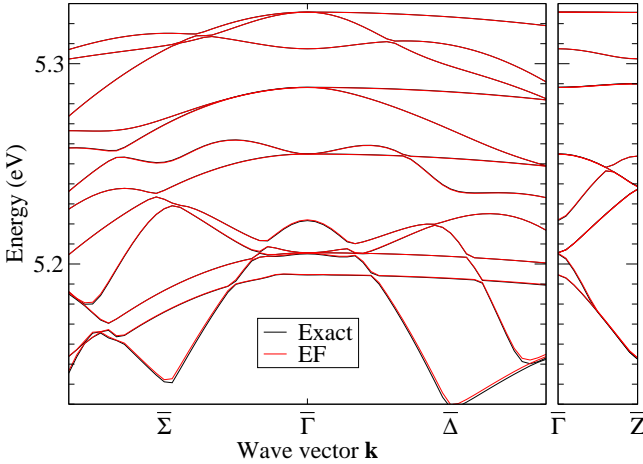


FIG. 21: (Color online) Valence band structure of a (001) $(\text{GaAs})_{24}(\text{Al}_{0.2}\text{Ga}_{0.8}\text{As})_{24}$ superlattice: comparison of exact and 3-state envelope-function (EF) calculations. The EF model is the same as that of Ref. 1, and the calculation includes 9 plane waves (PW). Symmetry labels are defined in Refs. 69 and 70; the Γ axis corresponds to the bulk Γ axis, and the border of the figure in the Γ direction is 6% of the distance to the bulk X point (the border in the Γ or bulk direction is the same physical distance).

conclude that the theory of Ref. 1 works very well in the weak-perturbation limit under which it was derived.

The following examples provide a more detailed study of the effects of various approximations in systems containing stronger perturbations. Figure 22 shows the top 12 valence subbands in a (001) $(\text{GaAs})_{24}(\text{AlAs})_{24}$ superlattice. The exact model calculations are compared here with a 283-state envelope-function model that includes all zone-center Bloch functions explicitly, corresponding to Fig. 20(a) in the bulk case. Figure 22(a) includes 25 plane waves in the envelope-function model. The results here are very accurate, with an error corresponding to about a 2 meV shift that is nearly the same for all subbands. This is the same as the quadratic error in the bulk Hartree potential shown in Figs. 15(c) and 18(b), which is almost the same as the quadratic error in the entire local potential. Figure 22(b) shows the effect of reducing the number of plane waves from 25 to 9. There is little change for energies close to the valence-band maximum, but the error in subband 12 is significant. Note that the energy range here is much wider than in Fig. 21, although it still corresponds approximately to the valence-band offset.

The effect of reducing set A to the 7 states in $_{15c}$, and $_{15v}$ is shown in Fig. 23. Part (a) is just the multiband theory of Ref. 1, the single-band version of which was used previously in Fig. 21. The results here are even slightly better than in Fig. 22(a), which can only be attributed to a fortuitous cancellation of errors. In part (b) the $O(k^4)$ terms are dropped. The results are still fairly accurate near the valence-band maximum; however, the peculiar behavior of (what should be) the ground state near Z shows that the plane-wave cuto

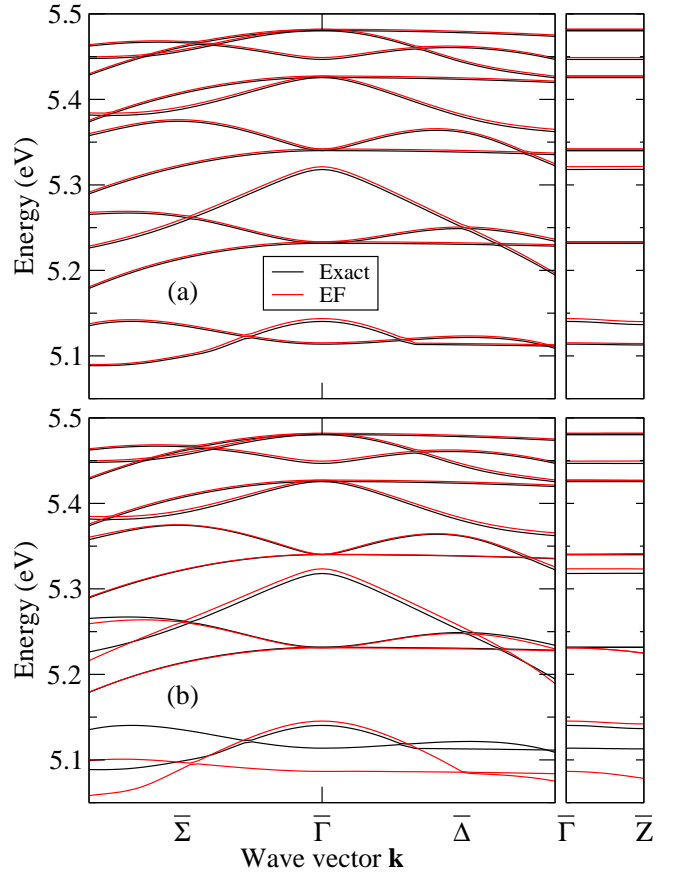


FIG. 22: (Color online) Valence band structure of a (001) $(\text{GaAs})_{24}(\text{AlAs})_{24}$ superlattice: comparison of exact and 283-state EF calculations. (a) 25 EF plane waves; (b) 9 EF plane waves. Both EF calculations use $O(k^4)$ bulk dispersion.

in this case is not quite sufficient to eliminate all effects of the $O(k^2)$ spurious solutions in Fig. 20(b). In Fig. 23(c) the $O(k^{2-1})$ terms are dropped, so that the mass and momentum matrices are approximated by those of the reference crystal. Here the error becomes significant even at fairly small energies, which shows the importance of including linear terms for multiband models.

In Figs. 24 and 25, the set A is reduced even further to only the three $_{15v}$ states. Figure 24 shows the bands on the same energy scale as before, while Fig. 25 shows an expanded view of the region near the band edge. Part (a) uses the linear mass model of Ref. 1 (the same as in Fig. 21). A close inspection of the top three subbands in Fig. 25(a) shows evidence of the errors in the linear mass approximation displayed in Table II. These errors are corrected in part (b), which includes quadratic corrections to the mass as well as (see Appendix D) terms of order k^4 in the potential. This yields a noticeable improvement, although the quantitative failure for higher excitations (due in large part to the use of only 9 plane waves) is still present. In part (c), the $O(k^4)$ terms are dropped; since spurious solutions are no longer a problem, the number of plane waves is increased to 25. It

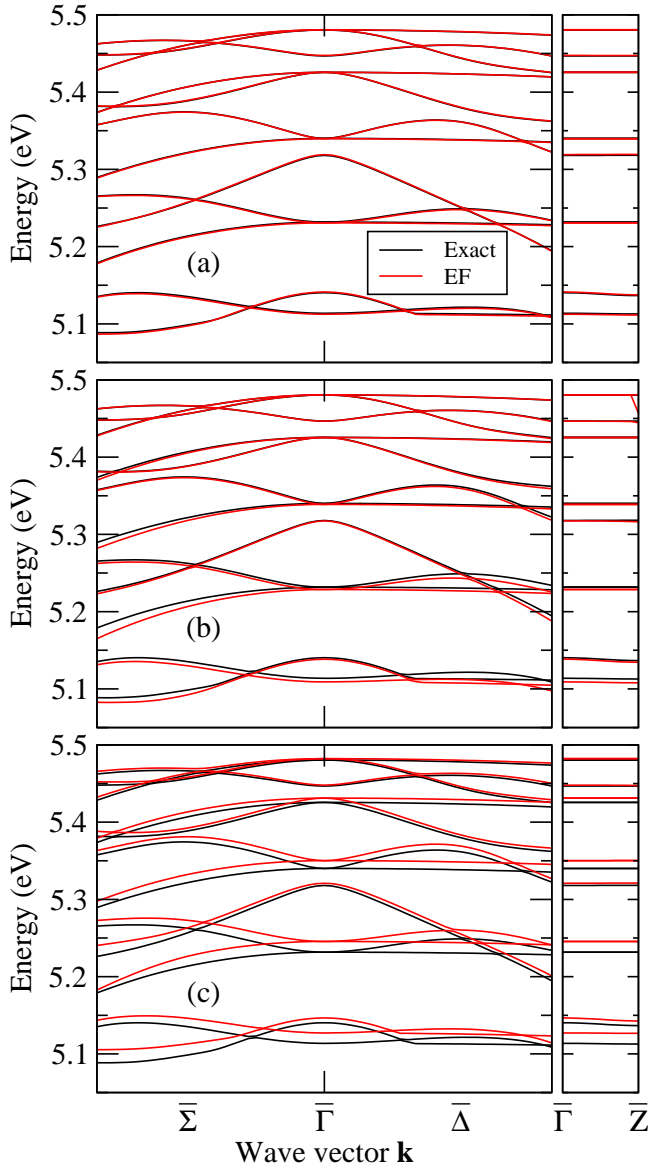


FIG. 23: (Color online) Valence band structure of a (001) $(\text{GaAs})_{24}/(\text{AlAs})_{24}$ superlattice: comparison of exact and 7-state EF calculations. The EF models are (a) $O(k^4/0 + k^2/1 + k^0/2)$; (b) $O(k^2/1 + k^0/2)$; (c) $O(k^2/0 + k^0/2)$. All EF calculations use 25 plane waves and $O(k^2)$ potentials.

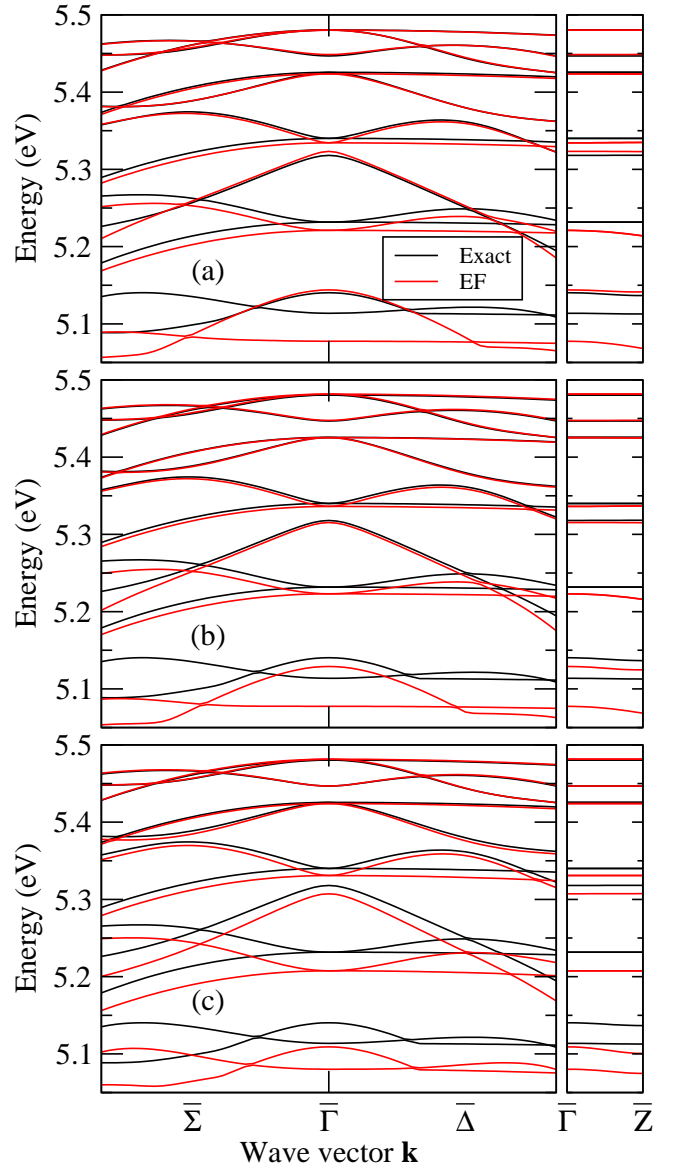


FIG. 24: (Color online) Valence band structure of a (001) $(\text{GaAs})_{24}/(\text{AlAs})_{24}$ superlattice: comparison of exact and 3-state EF calculations. The EF models are (a) $O(k^4/0 + k^2/1 + k^0/2)$, 9 PW; (b) $O(k^4/0 + k^2/2 + k^0/4)$, 9 PW; (c) $O(k^2/2 + k^0/4)$, 25 PW.

can be seen that the top three subbands are still quite accurate under this approximation.

Figure 26 shows the valence subband structure of a (001) $(\text{In}_{0.53}\text{Ga}_{0.47}\text{As})_{24}/(\text{InP})_{24}$ superlattice. Part (a) gives the results obtained from the original 283-state basis. The error here is somewhat larger than in the analogous calculation for GaAs/AlAs in Fig. 22(a), with most states shifted by about 6 meV. This is significantly more than the 2 meV bulk error in the quadratic approximation to the Hartree potential shown in Figs. 16(b) and 19(b). The 4 meV discrepancy is tentatively attributed to the interface error due to the truncation of

the linear multipole expansion shown in Fig. 19(b), although it is not clear why this should be significant for $\text{In}_{0.53}\text{Ga}_{0.47}\text{As}/\text{InP}$ but not for GaAs/AlAs.

In Fig. 26(b) the basis is reduced to 7 states using the linear mass renormalization of Ref. 1. The results are quite close to the exact calculation, although again the improvement over part (a) is fortuitous. This is demonstrated in part (c), which includes additional terms of order k^2 and k^4 . Most of the bands are shifted slightly upward, returning nearly to the result from part (a). The shift is mainly due to $O(k^3)$ corrections in the renormalized potential [see Eq. (11)].

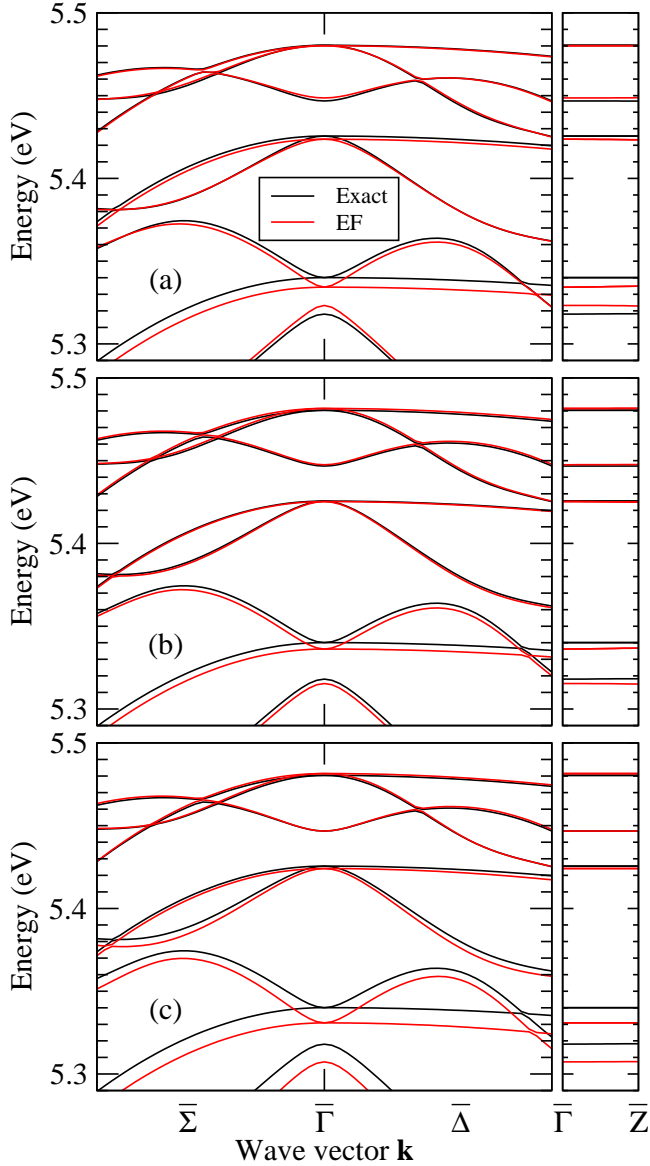


FIG. 25: (Color online) Expanded view of the top eight valence states from Fig. 24.

Figure 1 of Ref. 15 shows the results of calculations that are the same as Fig. 26(b), but for the 4-dimensional set $A = f_{1c}, 15v$. The results with $O(k^4)$ terms are almost identical to Fig. 26(b). The effect of dropping the $O(k^4)$ terms is somewhat more significant than in Fig. 23(b), however.

Finally, Fig. 27 shows the predictions of the single-band $15v$ model for $In_{0.53}Ga_{0.47}As/InP$. When $O(k^4)$ terms are included in the bulk Hamiltonian, the critical point of zero slope in the light-hole h100i dispersion is closer to than it was in GaAs/AlAs, so that now only 7 plane waves can be included in the envelope functions if one wishes to avoid spurious solutions. A part from this restriction, the envelope-function models used in parts (a), (b), and (c) of Fig. 27 are the same as

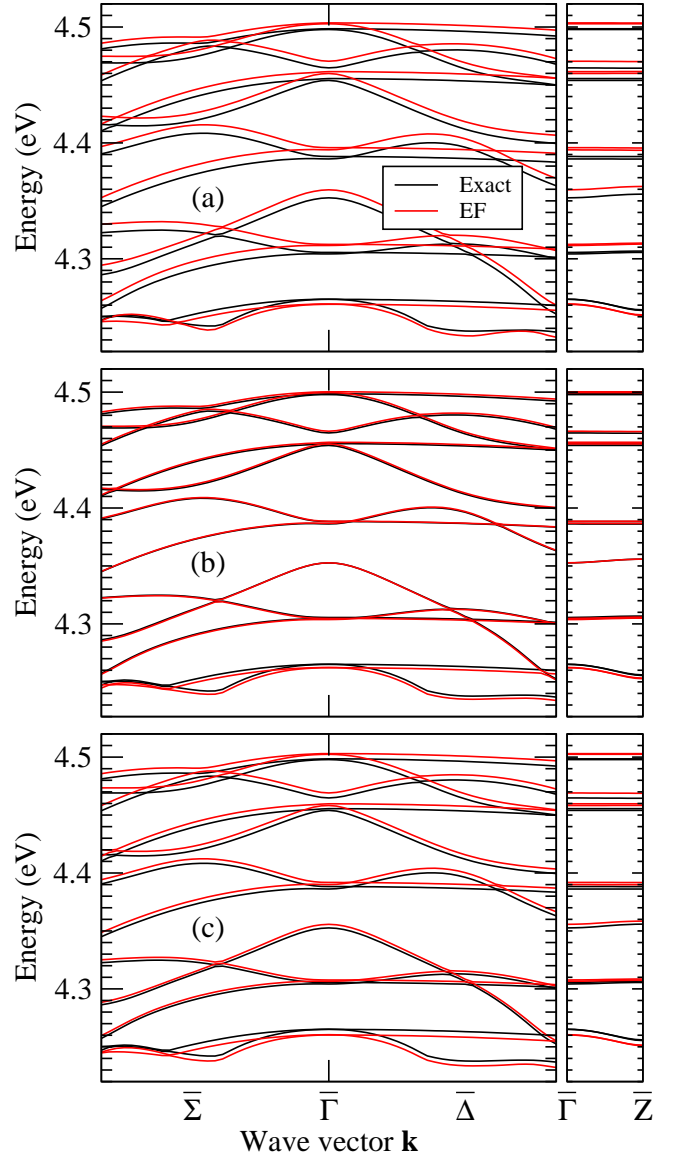


FIG. 26: (Color online) Valence band structure of a (001) $(In_{0.53}Ga_{0.47}As)_{24}/InP_{24}$ superlattice: comparison of exact and EF calculations. (a) 283-state EF model; (b) 7-state EF model, $O(k^{4/0} + k^{2/1} + k^{0/2})$; (c) 7-state EF model, $O(k^{4/0} + k^{2/2} + k^{0/4})$. All EF calculations use 25 plane waves and $O(k^4)$ bulk dispersion.

those used in the corresponding parts of Figs. 24 and 25. It can be seen that in this case the limitations of using only 7 plane waves are sufficiently severe that, for the first seven subbands, one is better off fitting the $O(k^4)$ terms and including more plane waves. It should be noted that the predictions of the single-band Hamiltonian for real $In_{0.53}Ga_{0.47}As/InP$ superlattices would likely be substantially worse than what is shown here (perhaps even qualitatively incorrect), since the energy gap of $In_{0.53}Ga_{0.47}As$ in the model system is 61% larger than the experimental value (see Sec. IIIA).

Although it is not visible on the scale of these g-

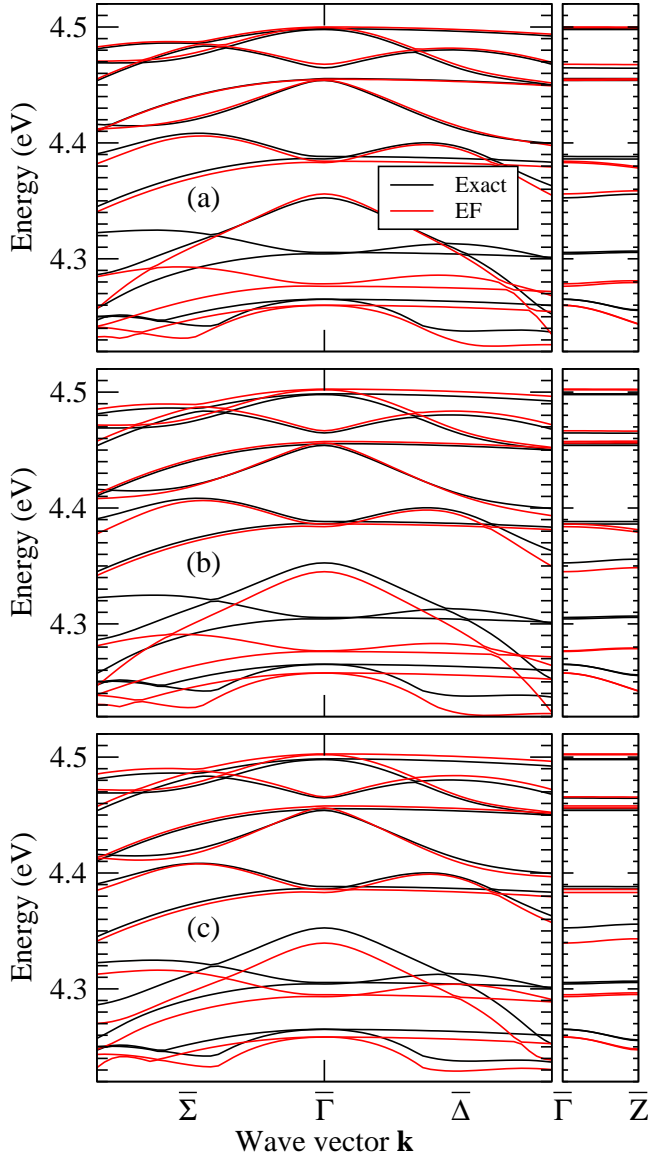


FIG. 27: (Color online) Valence band structure of a (001) $(In_{0.53}Ga_{0.47}As)_{24}/InP_{24}$ superlattice: comparison of exact and 3-state EF calculations. The EF models are (a) $O(k^4 + k^{2-1} + k^{0-2})$, 7 PW; (b) $O(k^4 + k^{2-2} + k^{0-4})$, 7 PW; (c) $O(k^{2-2} + k^{0-4})$, 25 PW.

ures, the double degeneracy of the ground state in $GaAs/AlAs$ is removed in $In_{0.53}Ga_{0.47}As/InP$ due to the reduction in symmetry from D_{2d} to C_{2v} . The primary cause of the splitting is mixing of the \mathbf{k}_1 and \mathbf{k}_2 valence states due to the short-range interface mixing in Eq. (27) and the long-range interface dipole potential in Fig. 10. The splitting of the quasidegenerate ground state calculated exactly and in various envelope-function models is presented in Table V. It can be seen that all of the envelope-function models give a reasonably good estimate of the splitting (which means that they provide a satisfactory description of the microscopic wave function in the interface region). However, when the diatomic

TABLE V: Splitting of the ground-state degeneracy in a (001) $(In_{0.53}Ga_{0.47}As)_{24}/InP_{24}$ superlattice.

Model	Diatom ic dipole included?	
	Yes	No
Exact	0.639 m eV	
EF (283 states)	0.722 m eV	
EF (7 states)	0.626 m eV	0.426 m eV
EF (3 states)	0.585 m eV	

dipole terms in Fig. 10 (and their associated polarization of the bulk reference crystal) are omitted, the splitting of the ground state in the 7-dimensional envelope-function model is reduced by about one third. This shows that the practice of fitting experimental splitting data to short-range interface terms only^{50,71,72} may give an incorrect description of the basic physics and overestimate the magnitude of the short-range terms.

VII. CONCLUSIONS

This paper has presented a numerical implementation of the first-principles envelope-function theory of Ref. 1 in a model system based on superlattice LDA calculations with momentum-conserving pseudopotentials. The electron density and potential energy of the superlattice were approximated by retaining only the linear and quadratic response to the heterostructure perturbation. This approximation worked very well, with an error of only about 2 m eV in typical III-V semiconductors.

The density and short-range potentials were then approximated further using truncated multipole expansions (i.e., power series in k), retaining terms of order k^2 in the linear potential and k^0 in the quadratic potential. This had no effect on the macroscopic density and potential in bulk, but it generated a significant additional error (due primarily to the truncation of the linear density response) in a narrow region near the interfaces. This error was not expected to have much effect on slowly varying envelope functions, which was confirmed by numerical examples (although it may have contributed about 4 m eV of error in $In_{0.53}Ga_{0.47}As/InP$ superlattices).

The approximate Hamiltonian was transformed from the original plane-wave basis to a Luttinger-Kohn basis using zone-center Bloch functions of the reference crystal. A Luttinger-Kohn unitary transformation was then used to eliminate the k -p and potential-energy coupling between the A states of interest and the remote B states. The resulting basis is material-dependent (due to the potential-energy terms) and approximates the position dependence of the Bloch functions in the heterostructure. The perturbation theory of Ref. 1 was extended to account for quadratic renormalization of the mass and momentum parameters.

A 7-state $f_{15v}, f_{1c}, f_{15c}g$ envelope-function model with linear momentum and mass renormalization

was shown to give a very good description of the valence subband structure of GaAs/AlAs and $In_{0.53}Ga_{0.47}As/InP$ (001) superlattices, although the good results were partly due to a fortuitous cancellation of errors. Calculations reported elsewhere¹⁵ show that similar results for 15_v can be obtained from a simpler 4-state $f_{15v}, 1c_g$ model. A 3-state 15_v model gave fairly good results over a more limited energy range (although it probably would not work as well in real $In_{0.53}Ga_{0.47}As/InP$ superlattices, since the energy gap of $In_{0.53}Ga_{0.47}As$ in the model system was significantly greater than the experimental value). The primary limitation of this single-band model is a conflict between the need for $O(k^4)$ bulk terms in order to achieve better accuracy in the excited states and the somewhat rather severe plane-wave cutoff needed to avoid spurious solutions generated by the $O(k^4)$ terms. The 3-state model did, however, give excellent results for GaAs/Al₂Ga_{0.8}As, where the band offset is small enough to satisfy Kohn's definition (~ 0.1 eV)³ of a shallow perturbation.

Dipole terms in the quadratic response were found to produce interface asymmetry and macroscopic electric fields in the no-communication atom $In_{0.53}Ga_{0.47}As/InP$ system. These terms, which have C_{2v} symmetry, produce a significant fraction of the splitting of the quasidegenerate ground state in such systems. Fitting this splitting to only short-range interface XY mixing terms may therefore overestimate the short-range terms and omit important physics.

Numerical results for $In_{0.53}Ga_{0.47}As/InP$ and GaAs/AlAs indicate that the linear valence-band Rashba coupling parameter is well approximated by the bulk effective Lande factor K for cationic perturbations, but that there is a wide disparity for anionic perturbations. Therefore, using bulk magnetooabsorption measurements to evaluate interface parameters such as the Rashba coupling^{73,74} cannot generally be relied upon to provide anything better than a rough order-of-magnitude estimate. Of course, the particular numbers generated by the present model would likely change significantly in a more realistic quasiparticle calculation, but the discrepancy between the Rashba and Lande coefficients is unlikely to vanish.

The operator ordering of the effective-mass terms at a heterojunction was found to be more complicated than in many previous models. Instead of having a single von Roos kinetic-energy operator of the form shown in Eq. (1), perturbation theory yields a linear combination of terms with all possible operator orderings. Certain terms are larger than others, however. As shown by Leibler,^{13,14} to linear order only the BenD aniel-Duke operator⁶² $T_{BD} = \frac{1}{2}pm^1p$ and the Gora-Williamson operator¹⁹ $T_{GW} = \frac{1}{4}(m^1p^2 + p^2m^1)$ arise. In a simple model where the matrix E_{nn} in Eq. (19) is assumed diagonal, the former arises in third-order perturbation theory from the position-dependent energies of remote bands in set B, whereas the latter comes from the position dependence of the bands in set A (see Appendix C). The Zhu{

Kroemer operator⁷⁵ $T_{ZK} = \frac{1}{2}m^{1=2}p^2m^{1=2}$ appears as one of several terms in quadratic renormalization, and the most general von Roos operator does not occur until cubic order.

Actually, with repeated use of the commutator $[p; f(z)] = i(df/dz)$, one can move the momentum operators into any desired position. For example, Morrow and Brownstein have shown that, upon replacing $\hat{p}^+ + \hat{p}^-$ and $\hat{p}^+ - \hat{p}^-$ in Eq. (1), the von Roos operator can be rewritten as¹⁸

$$T_{VR} = T_H - \frac{1}{2m} \frac{d[\ln(m)]^2}{dz}; \quad (32)$$

where $T_H = \frac{1}{2}pm^1pm^1$ is the Harrison operator⁷⁶ and the second term has the form of a potential energy. But one can continue this process indefinitely, for example by writing

$$T_H = T_{BD} - \frac{d}{dz} \frac{1}{2m} \frac{d[\ln(m)]}{dz} + \frac{1}{2m} \frac{d[\ln(m)]^2}{dz}; \quad (33)$$

Hence, the operator ordering in the effective kinetic energy is nothing but an arbitrary convention, as long as one takes care to retain all of the effective potential-energy terms generated by changing conventions.⁷⁷

The effective kinetic-energy operator given by the perturbation theory in this paper does have the advantage that the position-dependent functions (x) appearing in it are smooth step-like functions (although it should be noted that the position of the step is different for cations and anions). One could reduce it to the conventional BenD aniel-Duke form, or any other desired form, if one were willing to deal with functions having a more complicated position dependence near the interface.

This suggests that it may be possible (at least at the phenomenological level) to extend the perturbative scheme described here to arbitrarily high order in ϵ .⁷⁸ From this perspective, as long as (i) the bulk materials of the heterostructure are accurately described by an effective-mass equation and (ii) the heterostructure perturbation series eventually converges at some finite order, one can rearrange the operators into some standard order, yielding a standardized Hamiltonian with parameters that have a complicated but in principle calculable position dependence.

Of course, this is unlikely to provide a useful first-principles calculation method unless the series converges at a fairly low order. Fortunately, the examples given here demonstrate that linear (in the multiband case) or quadratic (in the single-band case) renormalization of the momentum and mass parameters is sufficient to achieve good results in several typical III-V heterostructures. Given that linear-response theory³⁸ has produced accurate predictions of valence-band offsets in many other lattice-matched and lattice-mismatched systems (see the bibliography of Ref. 1), it is likely that the present envelope-function theory can be applied successfully in many systems too.

ACKNOWLEDGMENTS

This work was supported by Hong Kong RGC Grant No. 600905.

APPENDIX A: PERTURBATION THEORY

This appendix defines a set of functions that offer a convenient way to describe operator ordering in fourth-order Luttinger-Kohn perturbation theory. These functions are merely an alternative way of writing the expressions given on p. 205 of Winkler's monograph.⁴⁷

In Luttinger-Kohn perturbation theory,^{2,5} the total Hamiltonian of the system is written as $H = H_0 + H^0$, where H_0 has matrix elements $(H_0)_{mn} = E_m \delta_{mn}$. The states of the unperturbed Hamiltonian H_0 are divided into a set A containing the states of interest, and a set B containing all other states. It is assumed that the energies of A and B do not overlap. A unitary transformation $H = e^S H e^S$ is used to eliminate the coupling between A and B to any desired order in the perturbation H^0 .

The notation used here is defined as follows. M_{AB} is the block of the matrix M that has rows in set A and columns in set B. The matrix G is defined by

$$(G_{AB})_{nn^0} = (E_n - E_{n^0})^{-1}; \quad G_{BA} = (G_{AB})^T; \quad (A1)$$

where T denotes the transpose. A dot indicates element-by-element multiplication of congruent matrices (which is easily implemented in Fortran90):

$$(A \cdot B)_n = A_{nn^0} B_{nn^0}; \quad (A2)$$

whereas juxtaposition denotes ordinary matrix multiplication.

The renormalized Hamiltonian H for states in A is given to fourth order in H^0 by⁴⁷

$$H_{AA} = H_{AA} + P_2(H^0; H^0) + P_3(H^0; H^0; H^0) + P_4(H^0; H^0; H^0; H^0); \quad (A3)$$

where the functions P_2 , P_3 , and P_4 are defined by

$$P_2(H^1; H^2) = \frac{1}{2} [(H_{AB}^1 \cdot G_B) H_{BA}^2 + H_{AB}^1 (G_{BA} \cdot \tilde{H}_{BA}^1)]; \quad (A4)$$

$$P_3(H^1; H^2; H^3) = \frac{1}{2} f[(H_{AB}^1 \cdot G_B) H_{BB}^2] \cdot G_B \cdot G_{BA}^3 + \frac{1}{2} H_{AB}^1 fG_{BA} \cdot \tilde{H}_{BA}^2 (G_{BA} \cdot \tilde{H}_{BA}^1) \cdot g + \frac{1}{2} f \tilde{H}_{AA}^1 (G_{AB} \cdot \tilde{H}_{BA}^1) \cdot G_B \cdot G_{BA}^3 + \frac{1}{2} H_{AB}^1 fG_{BA} \cdot [\tilde{H}_{BA}^2 \cdot G_A] H_{AA}^3 \cdot g; \quad (A5)$$

$$\begin{aligned} P_4(H^1; H^2; H^3; H^4) = & \frac{1}{2} H_{AA}^1 fG_{AB} \cdot [\tilde{H}_{BA}^2 (G_{AB} \cdot \tilde{H}_{BA}^1)] \cdot g \cdot G_B \cdot H_{BA}^4 \\ & + \frac{1}{2} H_{AB}^1 G_{BA} \cdot f[(H_{BA}^2 \cdot G_A) H_{AA}^3] \cdot G_A \cdot G_{BA}^4 \\ & + \frac{1}{2} H_{AB}^1 G_{BA} \cdot f[\tilde{H}_{BB}^2 (G_{BA} \cdot \tilde{H}_{BA}^1)] \cdot G_A \cdot G_{BA}^4 \\ & + \frac{1}{2} H_{AB}^1 G_{BA} \cdot H_{BB}^2 fG_{BA} \cdot [G_{BA}^2 \cdot G_A] H_{AA}^4 \cdot g \\ & + \frac{1}{2} H_{AA}^1 fG_{AB} \cdot [(\tilde{H}_{BA}^2 \cdot G_B) H_{BB}^3] \cdot g \cdot G_B \cdot H_{BA}^4 \\ & + \frac{1}{2} f \tilde{H}_{AA}^1 (G_{AB} \cdot \tilde{H}_{BA}^1) \cdot G_B \cdot G_{BA}^3 \cdot H_{BA}^4 \\ & + \frac{1}{3} f[(H_{AB}^1 \cdot G_B) H_{BA}^2] (G_{AB} \cdot \tilde{H}_{BA}^1) \cdot g \cdot G_B \cdot H_{BA}^4 \\ & + \frac{1}{3} H_{AB}^1 G_{BA} \cdot f[\tilde{H}_{BA}^2 \cdot G_A] H_{AB}^3 (G_{BA} \cdot \tilde{H}_{BA}^1) \cdot g \\ & + \frac{1}{6} f[(H_{AB}^1 \cdot G_B) H_{BA}^2] (H_{BA}^2 \cdot G_A) H_{AB}^3 \cdot G_B \cdot G_{BA}^4 \\ & + \frac{1}{6} f \tilde{H}_{AB}^1 (G_{BA} \cdot \tilde{H}_{BA}^1) (G_{AB} \cdot \tilde{H}_{BA}^1) \cdot g \cdot G_B \cdot G_{BA}^4 \\ & + \frac{1}{6} H_{AB}^1 fG_{BA} \cdot \tilde{H}_{BA}^2 (G_{AB} \cdot \tilde{H}_{BA}^1) (G_{BA} \cdot \tilde{H}_{BA}^1) \cdot g \\ & + \frac{1}{6} H_{AB}^1 fG_{BA} \cdot [(\tilde{H}_{BA}^2 \cdot G_A) (H_{AB}^3 \cdot G_B) H_{BA}^4] \cdot g \\ & + \frac{1}{24} (H_{AB}^1 \cdot G_B) (H_{BA}^2 \cdot G_A) (H_{AB}^3 \cdot G_B) H_{BA}^4 \\ & + \frac{1}{24} H_{AB}^1 (G_{BA} \cdot \tilde{H}_{BA}^1) (G_{AB} \cdot \tilde{H}_{BA}^1) (G_{BA} \cdot \tilde{H}_{BA}^1) \\ & + \frac{1}{8} (H_{AB}^1 \cdot G_B) (H_{BA}^2 \cdot G_A) H_{AB}^3 (G_{BA} \cdot \tilde{H}_{BA}^1) \\ & + \frac{1}{8} (H_{AB}^1 \cdot G_B) H_{BA}^2 (G_{AB} \cdot \tilde{H}_{BA}^1) (G_{BA} \cdot \tilde{H}_{BA}^1) \\ & + \frac{1}{2} f[(H_{AB}^1 \cdot G_B) H_{BB}^2] \cdot G_B \cdot G_{BA}^3 \cdot G_B \cdot H_{BA}^4 \\ & + \frac{1}{2} H_{AB}^1 G_{BA} \cdot H_{BB}^2 fG_{BA} \cdot \tilde{H}_{BA}^2 (G_{BA} \cdot \tilde{H}_{BA}^1) \cdot g : \end{aligned} \quad (A6)$$

This way of expressing H_{AA} is particularly useful when H^0 is a sum of operators that do not commute, and one wishes to keep track of the order of the various terms. In the present case, H^0 is a sum of k p terms and potential-energy matrix elements. Examples are given in the appendices below.

APPENDIX B: BULK RENORMALIZATION

In terms of the functions defined in Appendix A, the renormalized coefficients of order k^2 , k^3 , and k^4 in the bulk reference Hamiltonian for set A are given by¹

$$D_{AA}^{ij} = D_{AA}^{ij} + P_2(i; j); \quad (B1)$$

$$C_{AA}^{ijk} = C_{AA}^{ijk} + P_2(i; D^{jk}) + P_2(D^{ij}; k) + P_3(i; j; k); \quad (B2)$$

$$\begin{aligned} Q_{AA}^{ijkl} = & Q_{AA}^{ijkl} + P_4(i; j; k; l) \\ & + P_3(D^{ij}; k; l) + P_3(i; D^{jk}; l) + P_3(i; j; D^{kl}) \\ & + P_2(D^{ij}; D^{kl}) + P_2(i; C^{jk1}) + P_2(C^{ijk}; l) : \end{aligned} \quad (B3)$$

Here a tilde denotes a quantity before renormalization, which is obtained by fitting the reference Hamiltonian to a polynomial of order k^4 (as described in Sec. III E). The tilde is omitted on i because it does not change under renormalization.

APPENDIX C : LINEAR RENORMALIZATION

The terms in the renormalized Hartree operator that are linear in \mathbf{E} are given by¹

$$D_{AA}^{ij} = \tilde{D}_{AA}^{ij} + P_2(\tilde{E}^i; \tilde{E}^j); \quad (C1)$$

$$D_{AA}^{ij} = \tilde{D}_{AA}^{ij} + P_2(E^i; \tilde{E}^j); \quad (C2)$$

$$D_{AA}^{ij} = D_{AA}^{ij} + P_2(\tilde{E}^i; \tilde{E}^j) + P_2(E^i; D^{ij}) + P_3(E^i; \tilde{E}^j); \quad (C3)$$

$$D_{AA}^{ij} = D_{AA}^{ij} + P_2(\tilde{E}^i; \tilde{E}^j) + P_2(\tilde{E}^i; \tilde{E}^j) + P_3(\tilde{E}^i; \tilde{E}^j); \quad (C4)$$

$$D_{AA}^{ij} = D_{AA}^{ij} + P_2(\tilde{E}^i; \tilde{E}^j) + P_2(D^{ij}; E^i) + P_3(\tilde{E}^i; \tilde{E}^j); \quad (C5)$$

These are the same as the expressions given in Appendix C of Ref. 1, although written in a different notation. Once again, a tilde denotes a quantity before renormalization, which is obtained from a multipole expansion of the linear density and short-range potentials (Sec. III C) and from fitting the linear nonlocal potential to a polynomial of order k^2 (Sec. III E). The tilde is omitted on E because it does not change under renormalization.

APPENDIX D : QUADRATIC RENORMALIZATION

Perturbative renormalization also generates terms that are quadratic in E . The only term included in the Hartree operator of Ref. 1 was the renormalized potential

$$E_{AA} = P_2(E^i; E^j); \quad (D1)$$

Some of the present calculations also include quadratic renormalization of the momentum matrix:

$$D_{AA}^{ij} = P_2(E^i; \tilde{E}^j) + P_2(\tilde{E}^i; \tilde{E}^j) + P_3(E^i; E^j; \tilde{E}^j); \quad (D2)$$

$$D_{AA}^{ij} = P_2(E^i; \tilde{E}^j) + P_2(\tilde{E}^i; E^j) + P_3(E^i; \tilde{E}^j; E^j); \quad (D3)$$

$$D_{AA}^{ij} = P_2(\tilde{E}^i; E^j) + P_2(\tilde{E}^i; \tilde{E}^j) + P_3(\tilde{E}^i; E^j; \tilde{E}^j); \quad (D4)$$

and of the effective masses:

$$D_{AA}^{ij} = P_2(E^i; D^{ij}) + P_2(\tilde{E}^i; D^{ij}) + P_3(E^i; \tilde{E}^j; D^{ij}) + P_3(\tilde{E}^i; \tilde{E}^j; D^{ij}) + P_4(E^i; E^j; \tilde{E}^j); \quad (D5)$$

$$\begin{aligned} D_{AA}^{ij} &= P_2(\tilde{E}^i; \tilde{E}^j) + P_3(\tilde{E}^i; E^j; \tilde{E}^j) \\ &+ P_3(\tilde{E}^i; E^j; \tilde{E}^j) + P_3(\tilde{E}^i; \tilde{E}^j; \tilde{E}^j) \\ &+ P_4(\tilde{E}^i; E^j; \tilde{E}^j); \quad (D6) \end{aligned}$$

$$\begin{aligned} D_{AA}^{ij} &= P_2(D^{ij}; E^j) + P_2(D^{ij}; \tilde{E}^j) \\ &+ P_3(D^{ij}; E^j; E^j) + P_3(\tilde{E}^i; \tilde{E}^j; E^j) \\ &+ P_4(\tilde{E}^i; \tilde{E}^j; E^j); \quad (D7) \end{aligned}$$

$$\begin{aligned} D_{AA}^{ij} &= P_2(\tilde{E}^i; \tilde{E}^j) + P_2(E^i; D^{ij}) \\ &+ P_3(E^i; \tilde{E}^j; \tilde{E}^j) + P_3(E^i; \tilde{E}^j; E^j) + P_3(\tilde{E}^i; E^j; \tilde{E}^j) \\ &+ P_4(E^i; \tilde{E}^j; E^j); \quad (D8) \end{aligned}$$

$$\begin{aligned} D_{AA}^{ij} &= P_2(\tilde{E}^i; \tilde{E}^j) + P_2(D^{ij}; E^j) \\ &+ P_3(\tilde{E}^i; \tilde{E}^j; E^j) + P_3(\tilde{E}^i; \tilde{E}^j; \tilde{E}^j) + P_3(\tilde{E}^i; E^j; \tilde{E}^j) \\ &+ P_4(\tilde{E}^i; \tilde{E}^j; \tilde{E}^j); \quad (D9) \end{aligned}$$

$$\begin{aligned} D_{AA}^{ij} &= P_2(\tilde{E}^i; \tilde{E}^j) + P_2(D^{ij}; E^j) + P_2(E^i; D^{ij}) \\ &+ P_3(\tilde{E}^i; \tilde{E}^j; E^j) + P_3(E^i; D^{ij}; E^j) + P_3(E^i; \tilde{E}^j; \tilde{E}^j) \\ &+ P_4(E^i; \tilde{E}^j; \tilde{E}^j); \quad (D10) \end{aligned}$$

In these expressions, several approximations are used. Noting of the momentum and mass terms in the original quadratic Hartree operator was performed here; consequently, the unrenormalized parts are set to zero. Also, the term E^i is the mean unrenormalized diatomic short-range potential summed over all diatomic perturbations with the given values of E^i and E^j .

Some of the calculations also include renormalized short-range potential terms of order k^3 and k^4 , which were approximated using the expressions

$$E_{AA} = P_2(E^i; E^j) + P_2(E^i; \tilde{E}^j) + P_3(E^i; E^j; E^j); \quad (D11)$$

$$\begin{aligned} E_{AA} &= P_2(E^i; E^j) + P_3(E^i; E^j; E^j) \\ &+ P_3(E^i; \tilde{E}^j; E^j) + P_3(\tilde{E}^i; E^j; E^j) \\ &+ P_4(E^i; E^j; E^j); \quad (D12) \end{aligned}$$

Corrections of the same order arising from the long-range terms in the Hartree potential were neglected. For all of the numerical examples treated here, the $O(k^4)$ terms in Eq. (D12) were found to be negligible.

It should be emphasized that the results presented here do not provide a fully consistent perturbation scheme according to the criteria given by Takhtamirov and Volkov,⁷ in which the mean kinetic energy of the states of interest is assumed to be comparable to the heterostructure potential-energy perturbation. According to this scheme, if one includes the $O(k^2)$ and $O(k^3)$ terms shown

here, one should also include terms of order k^4 and k^6 .

However, since these require the use of sixth-order perturbation theory, such terms were judged to be not worth the effort in a preliminary investigation of this nature. Therefore, the results obtained by adding only the $O(k^2)$ and $O(k^4)$ terms are not expected to be valid for kinetic energies covering the full range of the band set, but only for kinetic energies small in comparison to the band set. This is indeed what was found in the numerical calculations of Sec. VI. Likewise, the $O(k^4)$ terms were found to be less important for states of small kinetic energy. These results are merely a reflection of the fact that a wide quantum well, unlike a hydrogenic impurity,⁵ does have states in which the mean kinetic energy is small compared to the mean perturbing potential. Thus, in this sense the theory of low-energy excitations of wide quantum wells is actually simpler than the corresponding theory of shallow impurities, because terms of high order in k are of lesser importance.

APPENDIX E: QUADRATIC RESPONSE

The method used here to handle the quadratic response differs slightly from that of Ref. 1. The quadratic potential response is given by Eq. (3.14) of Ref. 1:

$$V^{(2)}(x; x^0) = \frac{X^0 X^0}{R^0 R^0} V_{RR^0}(x; x^0); \quad (E1)$$

which has the same form as the quadratic density response in Eq. (7c). The translation symmetry of the reference crystal allows $V_{RR^0}(x; x^0)$ to be written as

$$V_{RR^0}(x; x^0) = V^{0; R^0 R}(x^0; x^0 R^0); \quad (E2)$$

in which R^0 is the midpoint of the two atoms:

$$R^0 = \frac{1}{2}(R + R^0 + \dots); \quad (E3)$$

In Eq. (E2), the coordinate reference is taken to be R^0 , whereas in Eq. (3.17) of Ref. 1, it was chosen to be $R + \dots$. The Fourier transform of Eq. (E1) is¹

$$V^{(2)}(k; k^0) = N \frac{X^0}{R^0 R^0} (k - k^0) v^{0; R^0}(k; k^0); \quad (E4)$$

where

$$v^{0; R^0}(k) = \frac{1}{N} \frac{X^0}{R^0 R^0} e^{ik(R^0 + (R^0 + \dots))} = 1; \quad (E5)$$

The coordinate reference (E3) is arbitrary, but it is sometimes more convenient for analyzing symmetry properties than the choice used in Ref. 1.

In the LDA model used here, the quadratic potential is local [i.e., $v^{0; R^0}(k; k^0) = v^{0; R^0}(k - k^0)$] since the ionic pseudopotential is purely linear. The diatomic potential $v^{0; R^0}(q)$ was approximated for small q by keeping only the dipole and quadrupole terms in the electron density and the $l=0$ term in the power-series expansion (11b) of the short-range potential (which in the quadratic case consists only of the exchange-correlation potential). For q near $G \neq 0$, only the $l=0$ terms were retained in both the density and short-range potential; see the end of Sec. IIIC for further remarks.

Electronic address: phbaff@ust.hk

- ¹ B. A. Foreman, Phys. Rev. B 72, 165345 (2005).
- ² J. M. Luttinger and W. Kohn, Phys. Rev. 97, 869 (1955).
- ³ W. Kohn, in *Solid State Physics*, edited by F. Seitz and D. Turnbull (Academic, New York, 1957), vol. 5, pp. 257–320.
- ⁴ L. J. Sham, Phys. Rev. 150, 720 (1966).
- ⁵ G. L. Bir and G. E. Pikkus, *Symmetry and Strain-Induced Effects in Semiconductors* (Wiley, New York, 1974); see x27 for corrections to elementary effective-mass theory.
- ⁶ M. G. Burt, J. Phys.: Condens. Matter 4, 6651 (1992).
- ⁷ E. E. Takhtamirov and V. A. Volkov, JETP 89, 1000 (1999).
- ⁸ J.-B. Xia, Phys. Rev. B 39, 3310 (1989).
- ⁹ L.-W. Wang, A. Franceschetti, and A. Zunger, Phys. Rev. Lett. 78, 2819 (1997).
- ¹⁰ L.-W. Wang and A. Zunger, Phys. Rev. B 56, 12395 (1997).
- ¹¹ L.-W. Wang and A. Zunger, Phys. Rev. B 59, 15806

(1999).

- ¹² L. V. Keldysh, Sov. Phys. JETP 18, 253 (1964).
- ¹³ L. Leibler, Phys. Rev. B 12, 4443 (1975).
- ¹⁴ L. Leibler, Phys. Rev. B 16, 863 (1977).
- ¹⁵ B. A. Foreman (2006), cond-mat/0612640.
- ¹⁶ O. von Roos, Phys. Rev. B 27, 7547 (1983).
- ¹⁷ R. A. Morrow and K. R. Brownstein, Phys. Rev. B 30, 678 (1984).
- ¹⁸ R. A. Morrow and K. R. Brownstein, Phys. Rev. B 31, 1135 (1985).
- ¹⁹ T. Gora and F. W. Billings, Phys. Rev. 177, 1179 (1969).
- ²⁰ M. C. Payne, M. P. Teter, D. C. Allan, T. A. Arias, and J. D. Joannopoulos, Rev. Mod. Phys. 64, 1045 (1992).
- ²¹ R. M. Martin, *Electronic Structure: Basic Theory and Practical Methods* (Cambridge University Press, Cambridge, 2004).
- ²² X. Gonze et al., Comput. Mater. Sci. 25, 478 (2002).
- ²³ X. Gonze et al., Z. Kristallogr. 220, 558 (2005).
- ²⁴ The ab init code is a common project of the Université Catholique de Louvain, Coming Incorporated, and other

contributors (URL <http://www.abinit.org>).

²⁵ C. H. Hartwigsen, S. Goeedecker, and J. Hutter, *Phys. Rev. B* 58, 3641 (1998).

²⁶ S. Goeedecker, M. Teter, and J. Hutter, *Phys. Rev. B* 54, 1703 (1996).

²⁷ W. G. Aulbur, L. Jonsson, and J. W. Wilkins, in *Solid State Physics*, edited by H. Ehrenreich and F. Spaepen (Academic, San Diego, 2000), vol. 54, pp. 1-218.

²⁸ G. Onida, L. Reining, and A. Rubio, *Rev. Mod. Phys.* 74, 601 (2002).

²⁹ B. A. Bernevig, T. L. Hughes, and S.-C. Zhang, *Phys. Rev. Lett.* 95, 066601 (2005).

³⁰ R. Resta, S. Baroni, and A. Baldereschi, *Superlattices Microstruct.* 6, 31 (1989).

³¹ S. Baroni, S. de Gironcoli, A. Dal Corso, and P. Giannozzi, *Rev. Mod. Phys.* 73, 515 (2001).

³² J. Ihm, A. Zunger, and M. L. Cohen, *J. Phys. C* 12, 4409 (1979); 13, 3095 (1980).

³³ M. T. Yin and M. L. Cohen, *Phys. Rev. B* 26, 3259 (1982).

³⁴ M. T. Yin and M. L. Cohen, *Phys. Rev. B* 26, 5668 (1982).

³⁵ G. Ortiz, R. Resta, and A. Baldereschi, *J. Phys.: Condens. Matter* 2, 10217 (1990).

³⁶ I. Vurgaftman, J. R. Meyer, and L. R. Ram-Mohan, *J. Appl. Phys.* 89, 5815 (2001).

³⁷ J. R. Chelikowsky and M. L. Cohen, *Phys. Rev. B* 14, 556 (1976); 30, 4828 (1984).

³⁸ S. Baroni, R. Resta, A. Baldereschi, and M. Peressi, in *Spectroscopy of Semiconductors and Microstructures*, edited by G. Fasol, A. Fasolino, and P. Lugli (Plenum, New York, 1989), vol. 206 of *NATO ASI Series B*, pp. 251-272.

³⁹ A. Baldereschi, S. Baroni, and R. Resta, *Phys. Rev. Lett.* 61, 734 (1988).

⁴⁰ The macroscopic averages^{41,42} were calculated by a method slightly different from that of Ref. 39. In addition to calculating a running average over a bulk unit cell, the functions were multiplied by a Gaussian momentum space to ensure that large wave-vector components were completely filtered out.

⁴¹ J. D. Jackson, *Classical Electrodynamics* (Wiley, New York, 1999), 3rd ed.

⁴² F. N. H. Robinson, *Macroscopic Electromagnetism* (Pergamon, Oxford, 1973).

⁴³ M. Peressi, S. Baroni, A. Baldereschi, and R. Resta, *Phys. Rev. B* 41, 12106 (1990).

⁴⁴ K. Kunc and R. Resta, *Phys. Rev. Lett.* 51, 686 (1983).

⁴⁵ R. G. Dandrea, C. B. Duke, and A. Zunger, *J. Vac. Sci. Technol. B* 10, 1744 (1992).

⁴⁶ B. A. Foreman, *Phys. Rev. B* 72, 165344 (2005).

⁴⁷ R. Winkler, *Spin-Orbit Coupling Effects in Two-Dimensional Electron and Hole Systems*, vol. 191 of *Springer Tracts in Modern Physics* (Springer, Berlin, 2003).

⁴⁸ J. M. Luttinger, *Phys. Rev.* 102, 1030 (1956).

⁴⁹ If one considers single atomic perturbations rather than planar perturbations, there are additional nonanalytic contributions from the linear octopole and hexadecapole moments of the electron density.¹ For the present case of planar perturbations, these are simply absorbed into the definition of the short-range potential using Eq. (14).

⁵⁰ E. L. Ivchenko, A. Yu. Kaminskii, and U. Rossler, *Phys. Rev. B* 54, 5852 (1996).

⁵¹ Y. R. Lin-Liu and L. J. Sham, *Phys. Rev. B* 32, R5561 (1985).

⁵² R. Eppenga, M. F. H. Schuurmans, and S. Colak, *Phys. Rev. B* 36, 1554 (1987).

⁵³ E. I. Rashba, *Sov. Phys. Solid State* 2, 1109 (1960).

⁵⁴ Yu. A. Bychkov and E. I. Rashba, *J. Phys. C* 17, 6039 (1984).

⁵⁵ R. Winkler, *Phys. Rev. B* 62, 4245 (2000).

⁵⁶ R. Winkler, H. Noh, E. Tutuc, and M. Shayegan, *Phys. Rev. B* 65, 155303 (2002).

⁵⁷ B. A. Foreman, *Phys. Rev. B* 48, R4964 (1993).

⁵⁸ C. R. Pidgeon and R. N. Brown, *Phys. Rev.* 146, 575 (1966).

⁵⁹ B. A. Foreman, *J. Phys.: Condens. Matter* 18, 1335 (2006).

⁶⁰ They could be obtained from analytical derivatives of the nonlocal pseudopotential in k space, but that was not done here since the primary focus of this paper is the physics of abrupt heterojunctions. The value of K also depends on the choice of coupling between the nonlocal potential and the magnetic field.⁵⁹

⁶¹ E. O. Kane, in *Narrow Gap Semiconductors: Physics and Applications*, edited by W. Zawadzki (Springer, Berlin, 1980), vol. 133 of *Lecture Notes in Physics*, pp. 13-31.

⁶² D. J. Bernal and C. B. Duke, *Phys. Rev.* 152, 683 (1966).

⁶³ G. Bastard, *Wave Mechanics Applied to Semiconductors and Heterostructures* (Wiley, New York, 1988).

⁶⁴ P.-O. Lowdin, *J. Chem. Phys.* 19, 1396 (1951).

⁶⁵ M. E. Flatte, P. M. Young, L.-H. Peng, and H. Ehrenreich, *Phys. Rev. B* 53, 1963 (1996).

⁶⁶ P. Pfeifer and W. Zawadzki, *Phys. Rev. B* 53, 12813 (1996).

⁶⁷ W. Yang and K. Chang, *Phys. Rev. B* 72, 233309 (2005).

⁶⁸ R. Dingle, W. Wiegmann, and C. H. Henry, *Phys. Rev. Lett.* 33, 827 (1974).

⁶⁹ L. J. Sham and Y.-T. Lu, *J. Lum.* 44, 207 (1989).

⁷⁰ G. F. Koster, in *Solid State Physics*, edited by F. Seitz and D. Turnbull (Academic, New York, 1957), vol. 5, pp. 173-256.

⁷¹ W. H. Lau and M. E. Flatte, *Appl. Phys. Lett.* 80, 1683 (2002).

⁷² F. Sznajdowicz, H. Haugan, and G. J. Brown, *Phys. Rev. B* 69, 155321 (2004).

⁷³ Rodina and Alekseev⁷⁴ have suggested dividing the heterostructure Hamiltonian into a bulk part and a surface part, in which the valence-band Rashba parameters for the bulk part are defined to be the same as the magnetic Luttinger parameters. However, since by symmetry the surface part contains terms with the same mathematical structure as the bulk part, this division does not carry any meaning unless one can make some definite statement about the magnitude of the surface part. As shown by the model calculations presented here, the surface part in this scheme is not generally negligible.

⁷⁴ A. V. Rodina and A. Yu. Alekseev, *Phys. Rev. B* 73, 115312 (2006).

⁷⁵ Q.-G. Zhu and H. Kwoerner, *Phys. Rev. B* 27, 3519 (1983).

⁷⁶ W. A. Harrison, *Phys. Rev.* 123, 85 (1961).

⁷⁷ K. Young, *Phys. Rev. B* 39, 13434 (1989).

⁷⁸ This scheme would be limited to the low-energy excitations of a wide quantum well or superlattice, as discussed in the remarks at the end of Appendix D.